Chapter 1

Introduction

Due to quite rapid growth of the wireless communication technologies and industries, each device in RF front end is required to have high performance and a small size. Filters are one of the essential components in the RF front end of modern wireless communication systems, such as mobile communication systems, satellite systems, and wireless network systems. Important performances of a bandpass filter include good frequency selectivity, compact size, high out-of- band rejection, and low insertion loss. Microstrip planar filters are usually preferred due to its low cost, good reliability and ease in design and fabrication.

The microstrip ring resonator has been widely used to evaluate phase velocity, dispersion, and effective dielectric constant of microstrip lines. Many applications, such as bandpass filters, oscillators, mixers, and antennas using ring resonators have been reported [1]. For years, the use of microstrip ring resonators for bandpass filter design has been widely studied. It can be attributed to some of its desirable properties such as low radiation loss, high quality factor and compact size. These bandpass filters built by dual-mode ring resonators were originally introduced by Wolff [2]. A dual-mode resonator consists of two degenerate modes, which are excited by perturbation-asymmetrical feed lines, added notches, stubs, or impedance step on the ring resonator. The coupling between the two degenerate modes is used to establish the bandpass. By proper arrangement of the perturbation, in addition to the excitation of the split modes, there are also two transmission zeros created at the both sides of the passband, such that a quasi-elliptic characteristic can be achieved.

Recently, many researches on ring filters have been published for innovative design or analysis methods [3-6], circuit miniaturization [7-11], and wide stopband properties [12-13]. In [3], *L*-shaped arms are used to enhance couplings and dual-mode excitations of quasi-elliptic function bandpass filters. Based on the transmission line theory, the even- and odd-mode analysis method in [4] is now popular for analysis of a dual-mode ring resonator possessing two ports spatially separated at 90^{o} and an impedance junction for perturbation at its symmetrical plane. In [5], the angle between input/output ports and the coupling between the dual modes are combined in formulation to control the attenuation pole frequencies. In [6], a joint field/circuit model is proposed to characterize line-to-ring coupling structures for design and optimization of microstrip ring resonator circuits.

Recently, many strategies have been developed for reducing area of a dual-mode ring filter. The loop resonator loaded with capacitive stubs in [7] and meander loop in [8] has a size reduction of more than 50%. In [9], a dual-mode resonator with a sophisticated pattern is designed to achieve a size reduction of 59%. In [10], a miniaturized dual-mode ring filter is designed with four equally spaced butterfly radial stubs. A new perturbation called local ground defect is included to make the orthogonal modes split up. A size reduction of better than 65% can be obtained. The etched holes in ground plane, however, need extra steps in circuit fabrication. In [11], two pairs of shunt capacitors are used to control the even and odd mode resonances for perturbation of the dual-mode ring filter. A size reduction of 55% - 67% is realized. Note that their circuit design involves lumped capacitors and via-holes.

Planar or quasi-planar bandpass filters suffer from unwanted responses in upper stopband due to the distributed nature and other circuit properties. The spurious response degrades not only the bandwidth of but also the rejection levels in the upper stopband. For widening the upper stopband, slow-wave open-loop resonators are

embedded into a square loop dual- mode resonator [12]. The spurious is detected at 2.5 times the design frequency. In [13], two topologies are proposed to suppress the unwanted harmonics. One intuitively connects 50-Ω spur-line bandstop filters at the I/O ports, and the other incorporates low-pass structures into the ring. Three circuits are presented for realizing the low-pass characteristics.

In this thesis, we propose two new miniaturized dual-mode ring resonator bandpass filters. In chapter 2, a capacitively-loaded square loop resonator is employed to design miniaturized dual-mode bandpass filters. The whole capacitively-loaded square loop resonator consists of four arrow-shape open stubs in a 2×2 configuration. The resonance characteristics of this resonator will also be investigated. The methods to introduce the optimum miniaturized resonators with perturbations for mode splitting and the ways of I/O excitation will be described.

In chapter 3, we propose a new fully planar microstrip periodic stepped-impedance ring resonator (PSIRR) bandpass filter. The design utilizes degenerate modes of a ring resonator consisting of a periodic cascade of hi-Z and low-Z sections. The proposed PSIRR has a compact area and a wide upper stopband with two transmission zeros. One of the zero can be tuned to suppress the first spurious so that the upper stopband can be extended up to 3.76 times the passband frequency.

Finally, conclusions will be drawn in Chapter 4.

Chapter 2

A New Miniaturized Dual-Mode Loop Filter

In the beginning of this chapter, a brief analysis of a uniform-impedance ring resonator is given. The analysis contains the basic resonance condition of a ring resonator. A new square loop resonator is then proposed for designing dual-mode bandpass filters. The center of each side of the resonator is tapped with a capacitive stub. As a result, the whole resonator encloses four coupled compact miniaturized hairpin resonators. The proposed dual-mode bandpass filter has not only a good stopband performance but also a size reduction of about 54%, as compared with a conventional dual-mode square loop bandpass filter. Besides, a parallel-line input/output structure is exploited to create an extra zero in upper stopband.

2.1 Uniform-Impedance Ring Resonators (UIRRs)

The ring resonator is merely a transmission line formed in a closed loop. The entire circuit consists of the feed lines, coupling gaps, and the resonator. Figure 2-1 shows one possible circuit arrangement. The signal power is coupled into and out of the resonator through feed lines and coupling gaps. If the distance between the feed lines and the resonator is large, the effect of the coupling gaps on the resonant frequencies of the ring is negligible. This type of coupling is a structure of loose coupling, which is a manifestation of the negligibly small capacitance of the coupling gap. If the feed lines are moved closer to the resonator, however, the coupling becomes tight and the gap capacitances become appreciable. This will cause the resonant frequencies of the circuit to deviate from the intrinsic resonant frequencies of the ring. It is worth mentioning that, however, the tight coupling structures can be exploited to reduce insertion loss in the passband for the design of ring bandpass filters.

When the mean circumference of the ring resonator is equal to an integer multiple of a guided wavelength, resonance is established. This may be expressed as following expression:

$$2\pi r = n\lambda_g \qquad \text{for } n = 1, 2, 3, \ldots \tag{2.1}$$

where r is the mean radius that equals the average of the outer and inner radii of the ring, λ_g is the guided wavelength, and n is the mode number. This relation is valid for the loose coupling case, as it does not take into account the coupling gap effect. For the first mode, maximum of field occur at the coupling gap location, and nulls occur 90° from the coupling gap locations.

For a microstrip ring, λ_g can be related to frequency by

$$\lambda_g = \frac{\lambda}{\sqrt{\varepsilon_{eff}}} = \frac{1}{\sqrt{\varepsilon_{eff}}} \frac{c}{f} \tag{2.2}$$

where c is the speed of light and ε_{eff} is the effective dielectric constant.From (2.1), the resonant frequency can be written as

$$f = \frac{nc}{2\pi r \sqrt{\varepsilon_{eff}}} \qquad \text{for } n = 1, 2, 3, \ldots \tag{2.3}$$

Figure 2-2 shows the simulated resonant frequencies of the leading five modes of an UIRR using loose coupling with outer radius r_o = 12.3 mm and inner radius r_i = 11.7 mm on a substrate with dielectric constant 10.2. The simulator was the software package IE3D [14].

2.2 Development of the resonator

The proposed new square loop resonator is shown in Figure 2-3. The development of this resonator is described as follows. Figure 2-4(a) shows three resonators, namely, resonators A, B, and C. Resonator A is a square loop resonator, and its fundamental resonant frequency can be predicted by that the mean circumference equals one guided wavelength. Four open stubs are then tapped at the centers of the four sides of resonator A to make up resonator B [7]. The structure is symmetric about a horizontal plane connecting two diagonal corners of the square loop. The conditions for determining even- and odd-mode resonant frequencies of resonator B can be formulated by using transmission line equations. Conceptually, in its equivalent circuit, the open-circuited arms bring out additional capacitive loads on equivalent circuit of the resonator, thereby reduce the resonant frequency and increase width of

upper stopband at the same time [9]. By further extending these stubs at the open ends and making V-shape stubs, resonator C is built up as shown in Figure 2-4(a). Compared with the stubs in resonator B, the V-shape stubs together with the resonator C is supposed to have more capacitance to further reduce the overall size of the resonator. Note that all the three resonators have two degenerate modes.

The fundamental resonant frequencies of the three loop resonators are investigated by the commercial EM simulator IE3D [14]. Through a loose coupling scheme shown in Figure 2-4(a), simulated $|S_{21}|$ responses for the three resonators are plotted in Figure 2-4(b). The detailed dimensions of the circuits are given with the circuit in Figure 2-4(a), and the circuit substrate has ε_r =10.2 and thickness = 1.27mm. Resonator A shows a resonant frequency at f = 3.7 GHz. When an open stub of 2.7 mm is attached to the center of each side, the $|S_{21}|$ response indicates that the resonant frequency of resonator B locates at 3.3 GHz. For resonator C, the resonant frequency keeps on decreasing as the length of the V-shape stubs is increased. When the length of a V-shape stub is 0.8 mm, the resonant frequency locates at 2.93GHz. It means that the size of the loop resonator can be successfully reduced by the arrow-shape open stubs.

2.3 Analysis of the arrow-shape open stubs

Consider only a quarter section of Figure 2-3 which consisting of a arrow-shape stub. The circuit plotted again in Figure 2-5(a) and its equivalent transmission line model is in Figure 2-5(b). Figure 2-5(c) shows a transmission line resonator loaded with a capacitor at it center, which can be the equivalent circuit of Figure 2-5(b) since the arrow-shape stub is equivalent to a capacitive load. From Figure 2-5(b) and Figure 2-5(c), the input characteristic admittances looking to the load at the tap point, Y_C' and Y_C can be expressed as the following

$$Y_C^{'} = j\omega Y_2 \frac{2\tan\theta_1 + R\tan\theta_2}{R - 2\tan\theta_1\tan\theta_2} \quad , \quad R = \frac{Z_1}{Z_2} \tag{2.4}$$

$$Y_C = j\omega C \tag{2.5}$$

By setting $Y_C^{'}$ in (2.4) identical to Y_C in (2.5), we have

$$C = \frac{Y_2}{\omega} C^{'} \tag{2.6}$$

$$C^{'} = \frac{2\tan\theta_1 + R\tan\theta_2}{R - 2\tan\theta_1\tan\theta_2} \tag{2.7}$$

where $\theta_1 = \beta l_1$, $\theta_2 = \beta l_2$, β is the phase constant of uniform impedance ring resonator. Figure 2-6 plots the effective capacitive load factor C' with respect to the length ratio of arrow-shape stubs $\theta_1 / (\theta_1 + \theta_2)$ for R =0.7, 0.8,1 and 1.2 and $\theta_1 + \theta_2 = 0.25\ \pi$. It can be observed that in order to obtain a large C', the impedance ratio R should be smaller than one and C' is increased as R is decreased for a given Z_2. Besides, it indicated that as the length ratio of arrow-shape stubs $\theta_1 / (\theta_2 + \theta_1)$ is about 0.7, C' has a maximum for each R. Several cases are simulated on the substrate with ε_r =10.2 and thickness = 1.27mm by the commercial EM simulator IE3D to demonstrate the analysis.

(1) Case A- Resonant characteristics for different lengths of the stubs

In this case, the length of arrow-shape stubs l_1 is increased and l_2 is fixed. In Figure 2-7(a), the increase of l_1 is supposed to increase the loading equivalent capacitance. Figure 2-7(b) plots the simulated resonant characteristics of the capacitively-loaded

square loop resonators for l_1 = 0.8, 1.8 and 2.8 mm and R=1. It is found that the closer the length ratio $\theta_1/(\theta_2+\theta_1)$ to 0.7, the lower the fundamental frequency of the loop resonator. When l_1 = 2.8 mm, the $|S_{21}|$ response indicates that the resonant frequency of resonator C locates at 2.82 GHz. The frequency reduction is 24% as compared with the frequency of resonator A shown in Figure 2-4(b). In other words, for circuit design, at the same frequency, a size reduction of $1-(2.82/3.7)^2\times$ 100% or 42% is achieved as compared with resonator A.

(2) Case B- Resonant characteristics for different impedance ratios of the stubs

In this case, the impedance ratio of arrow-shape stubs *R* is decreased for a fixed l_1+l_2. As shown in Figure 2-8(a), the decrease of *R* is again supposed to increase the equivalent loading capacitance. Figure 2-8(b) plots the simulated resonant characteristics of the capacitively-loaded square loop resonators for R =1, 0.85 and 0.7 and l_1+l_2 = 6.9 mm. It is found that the smaller the impedance ratio *R* is, the more the fundamental frequency of the loop resonator can be reduced. When R = 0.7, the $|S_{21}|$ response indicates that the resonant frequency of resonator C locates at 2.34 GHz. The frequency reduction is 37% as compared with the frequency of resonator A shown in Figure 2-4(b). In other words, at the same frequency, there is a size reduction of $1-(2.34/3.7)^2\times$ 100% or 60% as compared with resonator A.

From the simulation results of case A and case B, it is found that the range of the frequency reduction depends on not only the lengths of the arrow-shape stubs, but also the impedance ratio of transmission line l_1 and l_2. It is noted that the free area inside a loop is limited by the loop circumference, so there are restrictions on the stubs length and the value of the impedance ratio.

2.4 Dual-Mode Resonator

As shown in Figure 2-3, a small square patch of sizes $d\times d$ as a perturbation element

is attached to the center of the V-shape stub. The degenerate modes of the resonator are named as Mode-I and Mode-II. These two modes are excited and coupled to each other due to the perturbation element. When there is no perturbation (d = 0), only a single resonant frequency will be detected. Figure 2-9 shows the current density patterns of the resonant modes obtained by the IE3D. From the patterns, it can be clearly observed that one zero current locates at upper right and the other at lower left corner, and one pole at upper left and the other at lower right corner of the resonator. If the excitation is switched to port 2, the current density is rotated by 90°.

Figure 2-10 shows the simulated current densities when the perturbation has d = 0.96. It can be seen that the locations of poles and zeros of Mode-I and those of Mode-II rotated by 90°. It can be anticipated that the larger the perturbation, the larger the coupling between the two modes. The coupling leads the degenerate resonances to be split up into two frequencies, f_1 and f_2. For observing the mode splitting, the dual-mode resonator is simulated with different perturbation sizes, and the results are in Figure 2-11. The frequencies of Mode-II are nearly independent of d, while those of Mode-I decrease rapidly as d is increased. The coupling coefficient between the two modes can be calculated as [5]

$$K = 2\frac{|f_1 - f_2|}{f_1 + f_2} \tag{2.8}$$

The coupling coefficient as a function of d is also plotted in Figure 2-11.

2.5 Simulation and Measurement

Two dual-mode microstrip bandpass filters were fabricated on substrates having ε_r = 10.2 and thickness = 1.27 mm. For the first filter, the dimensions (mm) are a = b =

9.05, d = 0.96, w_1 = w_2 = 0.7, w_3 = 0.88, s = 0.2, l_1 = 2.48, l_2 = 2.32 and g = 0.25. The impedance ratio R and length ratio $\theta_1 / (\theta_2 + \theta_1)$ are 0.9 and 0.48, respectively. The input and output ports are spatially separated at 90°. Figure 2-12(a) shows the simulated and measured frequency responses. At center frequency 2.45GHz, the simulation fractional bandwidth is 3.4%, while the measured bandwidth is 3.3%. The insertion loss is 2.47 dB, and the return loss in passband is better than 20dB. Figure 2-12(b) shows the responses in a broad frequency band and 2-12(c) is the circuit photograph. The second fiter dimensions (mm) are a = b = 8.37, d = 0.95, w_1 =0.91, w_2 = 0.28, w_3 = 1.05, s = 0.18, l_1 = 2.19, l_2 = 2.13 and g = 0.27. The impedance ratio R and length ratio $\theta_1 / (\theta_2 + \theta_1)$ are 0.62 and 0.5, respectively. The input and output ports are spatially separated at 90°. Figure 2-13(a) shows the simulated and measured frequency responses. At center frequency 2.38GHz, the simulation fractional bandwidth is 3.3%, while the measured bandwidth is 3%. The insertion loss is 2.56 dB, and the return loss in passband is better than 20dB. Figure 2-13(b) shows the responses in a broad frequency band and 2-13(c) is the circuit photograph. The simulated and measured results are in good agreement.

Compared with the dual-mode filter presented in [2]-[4], our filters exhibit a wide stopband with a rejection level better than 22 dB up to 5GHz, and a deep transmission zero at two times the fundamental frequency. The frequency of the zero is determined by treating the input feeder as a quarter-wave open stub. When the input impedance at the tap point of port #1 is virtually short-circuited, the frequency is a zero. It can be anticipated that the zero can be tunable by changing the length of feeders. In addition, the dual-mode filter has an advantage that the center frequency can be adjusted by changing the length of the V-shape stubs ℓ_2. Finally, it is worth mentioning that the dimensions of the two dual-mode filters are 9.05×9.05 mm^2 and 8.37×8.37 mm^2

which are only about 45% and 38%, respectively, of that of a conventional closed loop resonator shown in Figure 2-4(a).

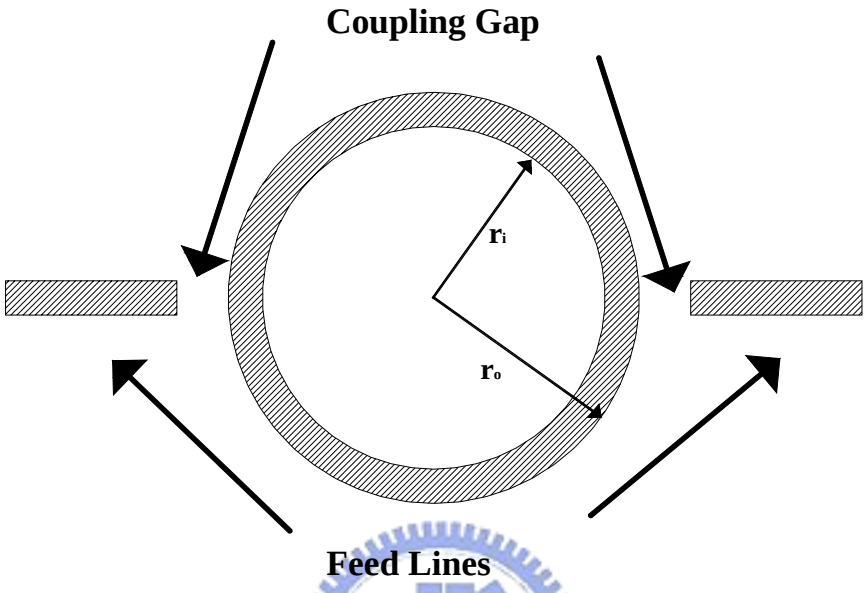

Figure 2-1 The uniform impedance microstrip ring resonator with feed lines

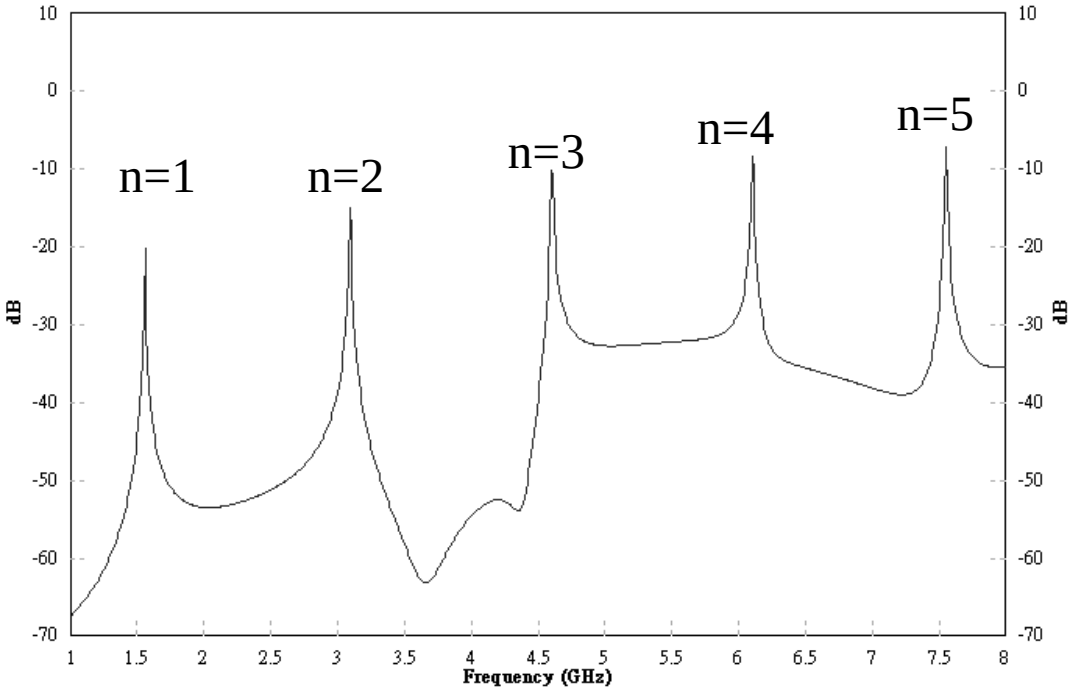

Figure 2-2 Simulated resonant characteristic of the UIRR in Figure 2-1 for n = 1 to 5.

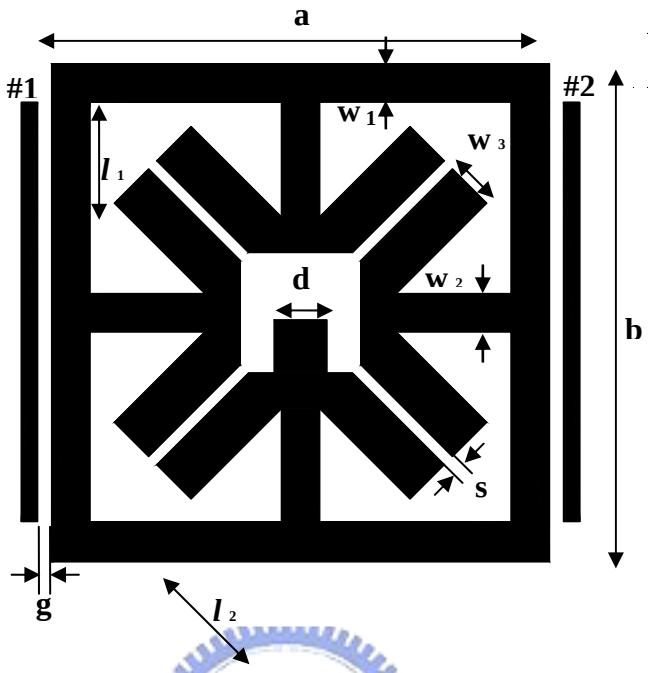

Figure 2-3 The proposed capacitively-loaded dual-mode filter

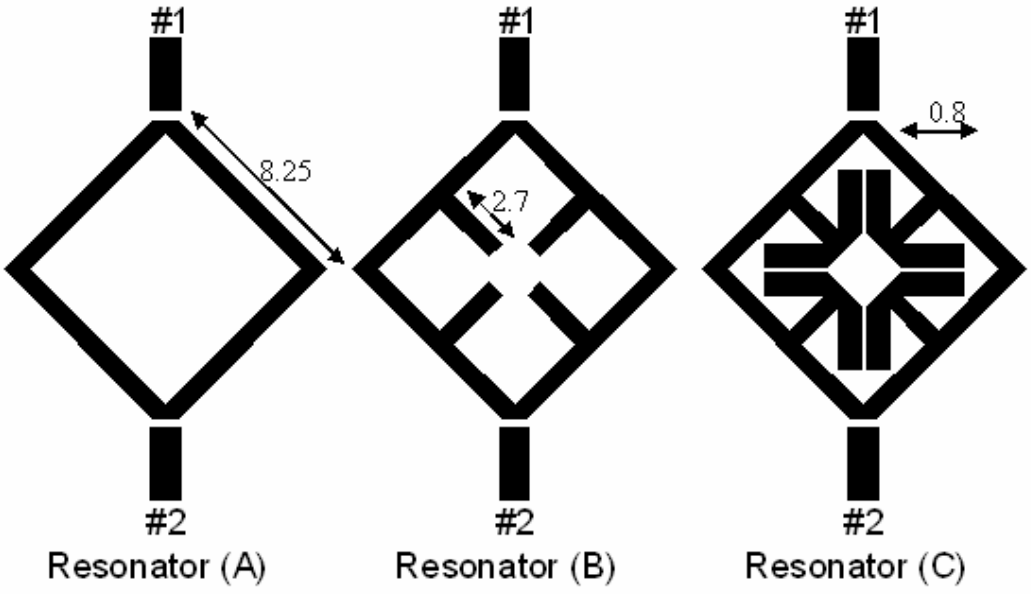

(a)

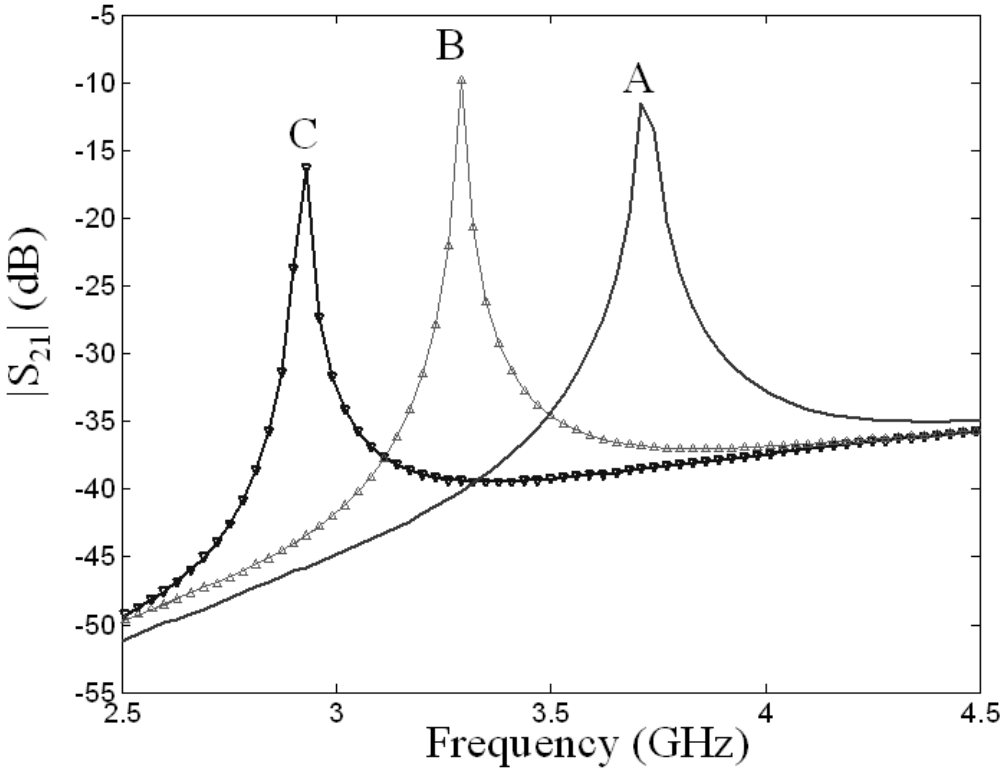

(b)

Figure 2-4 Layouts and resonant behaviors of the three square loop resonators with or without arrow-shape stubs. (a) Layouts. (b) Test of resonant frequencies of resonators A, B, and C.

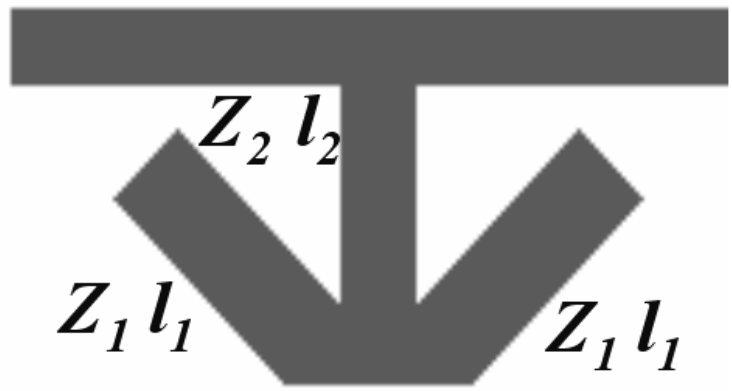

(a)

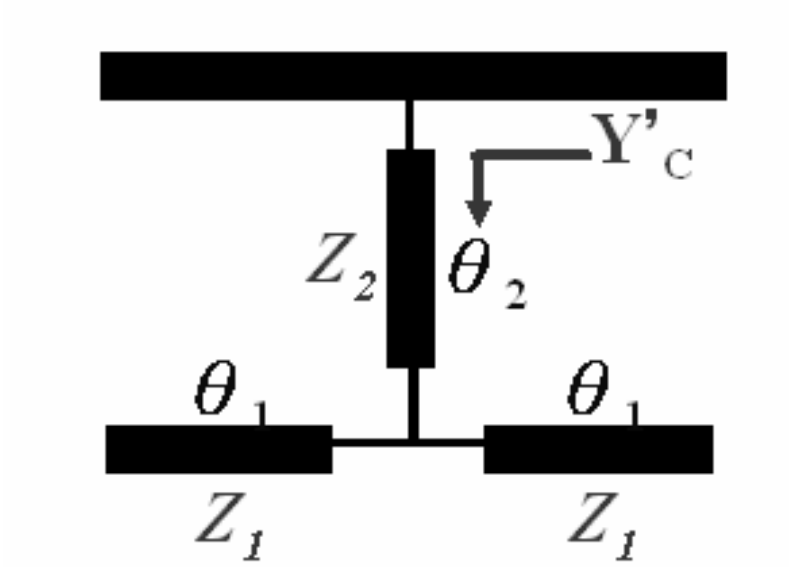

(b)

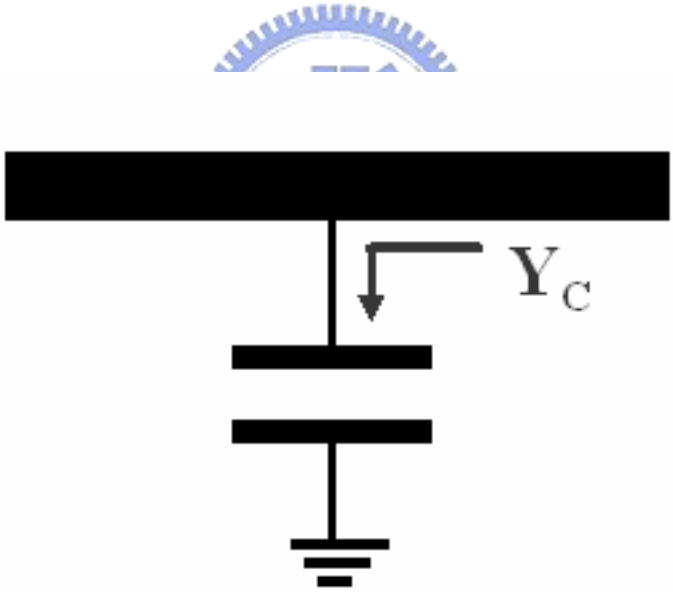

(c)

Figure 2-5 (a) A quarter section of the capacitvely-loaded square loop resonator. (b) Its equivalent circuit. (c) A capacitvely loaded transmission line resonator.

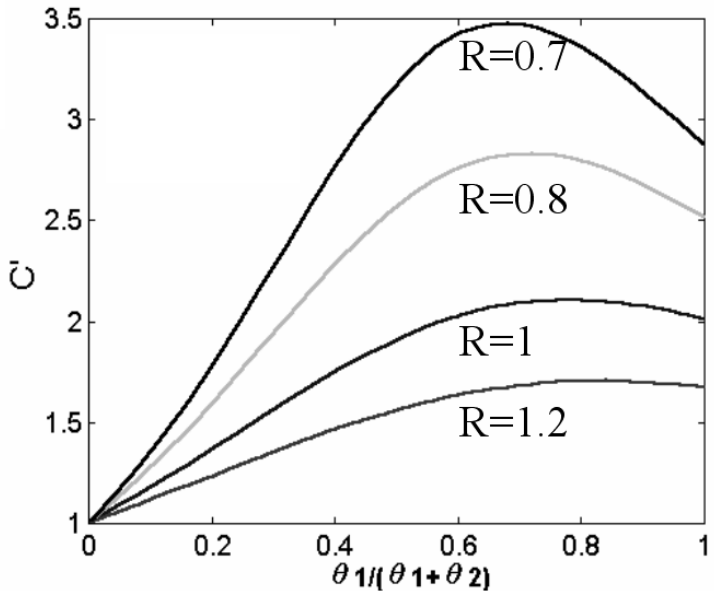

Figure 2-6 The effective capacitive load factor of varying length ratio and impedance ratio of arrow-shape stub.

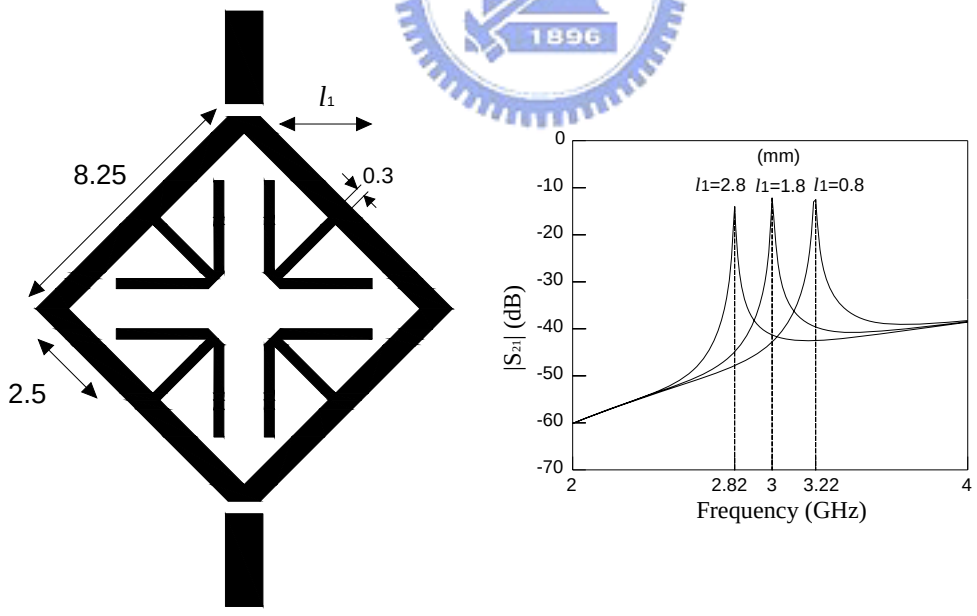

(a) (b)

Figure 2-7 Layouts and resonant behaviors of the square loop resonators with arrow-shape stubs for different l_1. (a) Layouts. (b) Frequency responses

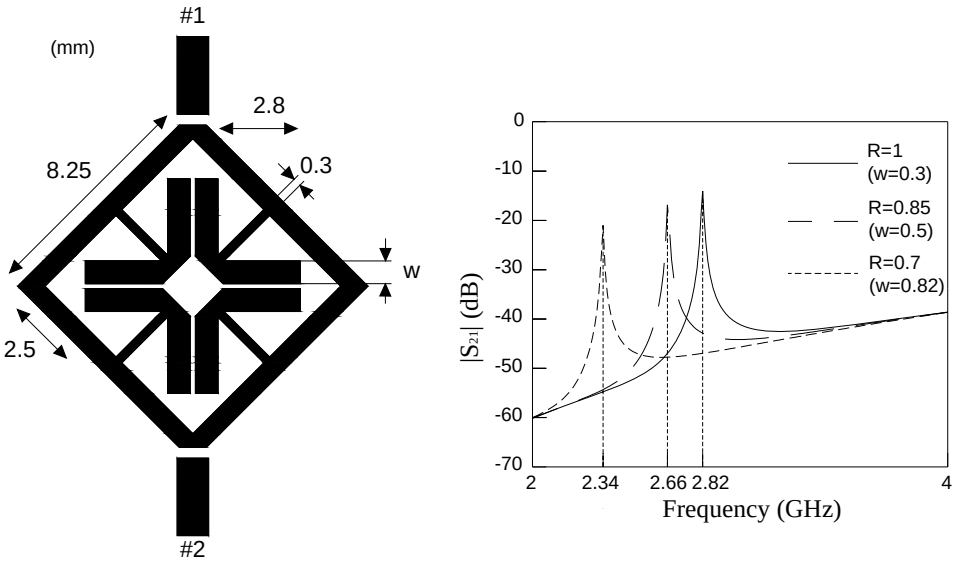

(a) (b)

Figure 2-8 Layouts and resonant behaviors of the square loop resonators with arrow-shape stubs for different impedance ratio R. (a) Layouts. (b) Frequency responses

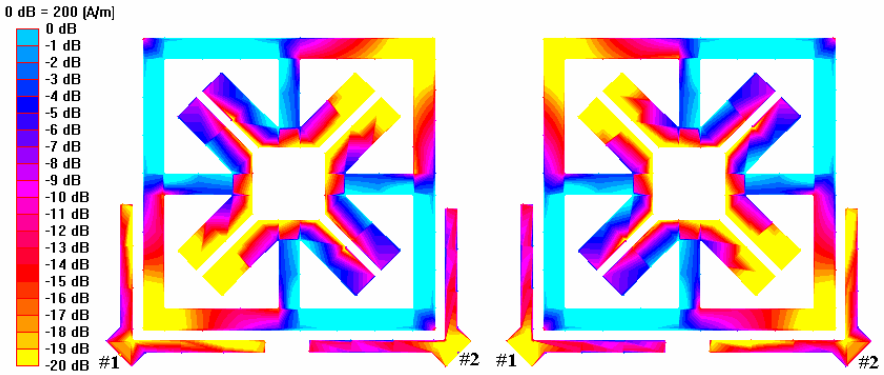

(a) (b)

Figure 2-9 Simulated current density patterns at resonant frequency f = 2.46GHz with d = 0. (a) Excited at port #1. (b) Excited at port #2.

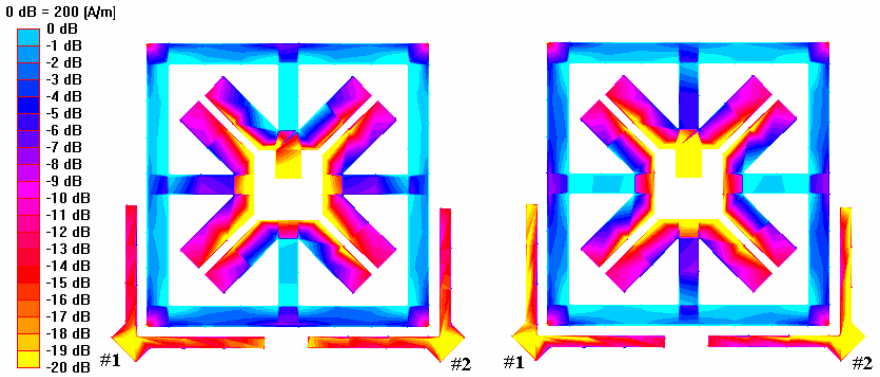

(a) (b)

Figure 2-10 Simulated current densities at resonances with d = 0.96. (a) Mode-I at f = 2.447GHz. (b) Mode-II at f = 2.492GHz.

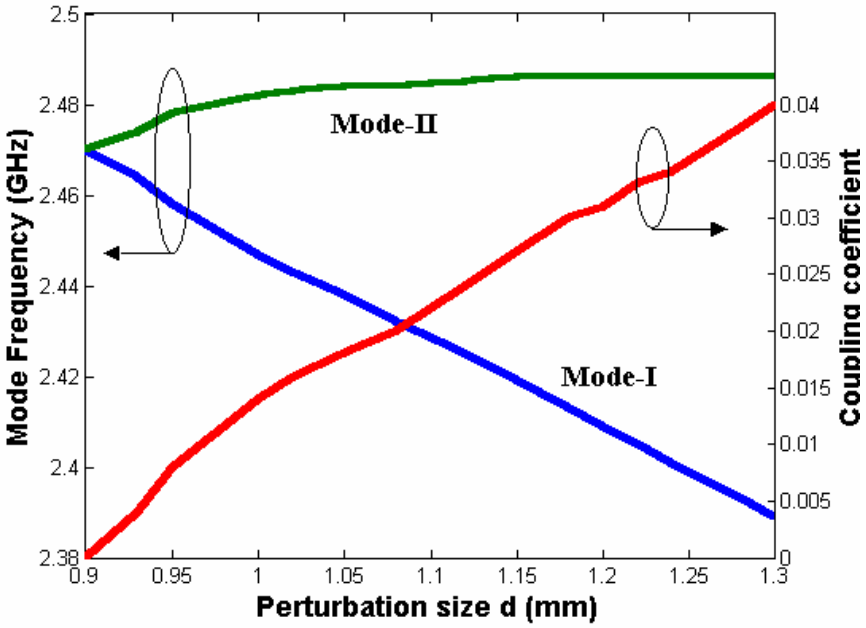

Figure 2-11 Simulated resonant frequencies of the two degenerate modes and their coupling coefficients versus perturbation size d. Referred to Fig.2-3, dimensions of the resonator (mm) are a = b = 9.05 mm, w_1 = w_2 = 0.7 mm, w_3 = 0.88mm, s = 0.2mm, l_1 = 2.08 mm, l_2 = 2.32 mm, g = 0.25 mm.

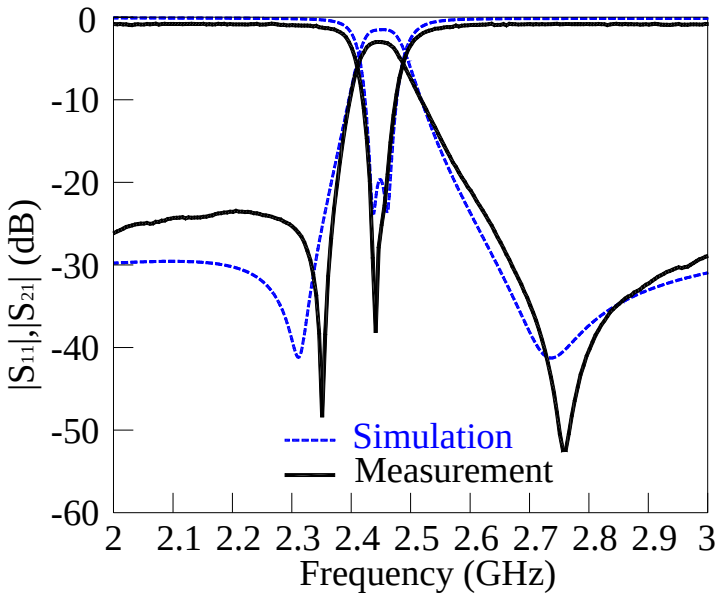
0
-10
-20
-30
-40
-50
-60
|S11|,|S21| (dB)
Simulation
Measurement
2
2.1
2.2
2.3
2.4
2.5
2.6
2.7
2.8
2.9
3
Frequency (GHz)

(a)

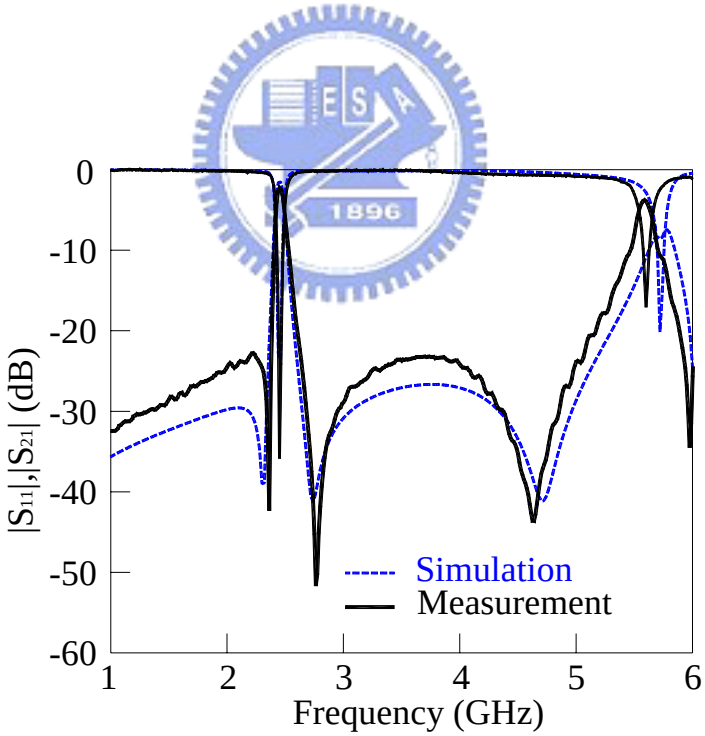
0
-10
-20
-30
-40
-50
-60
|S11|,|S21| (dB)
Simulation
Measurement
1
2
3
4
5
6
Frequency (GHz)

(b)

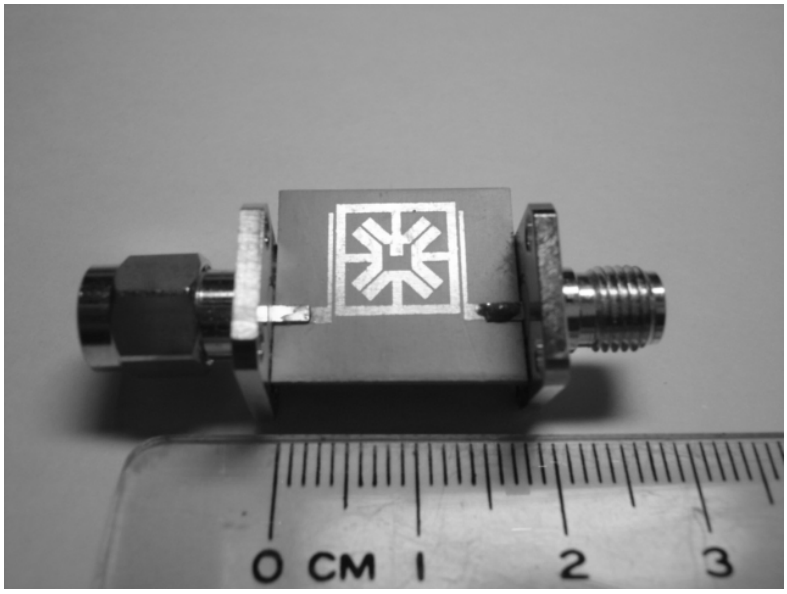

(c)

Figure 2-12 Simulated and measured filter responses for R=0.9 in (a) a narrow band, (b) broadband and (c) circuit photo.

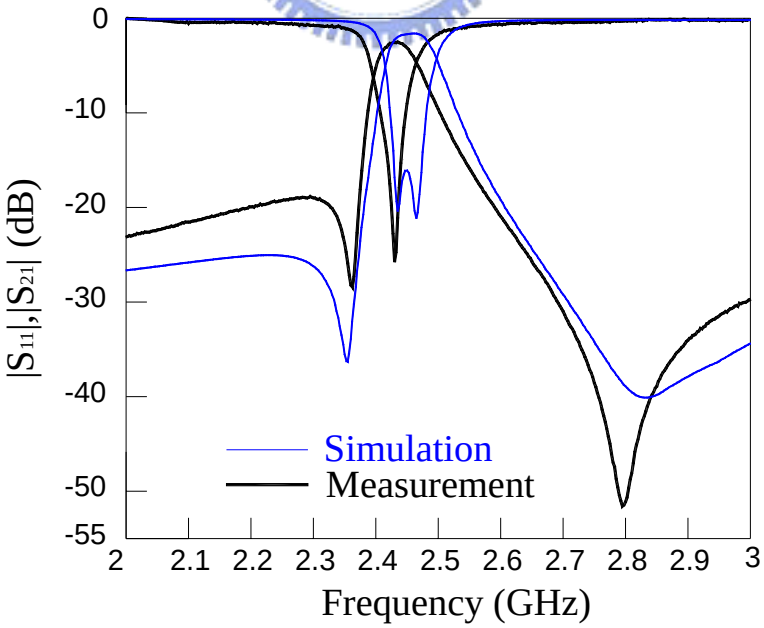

(a)

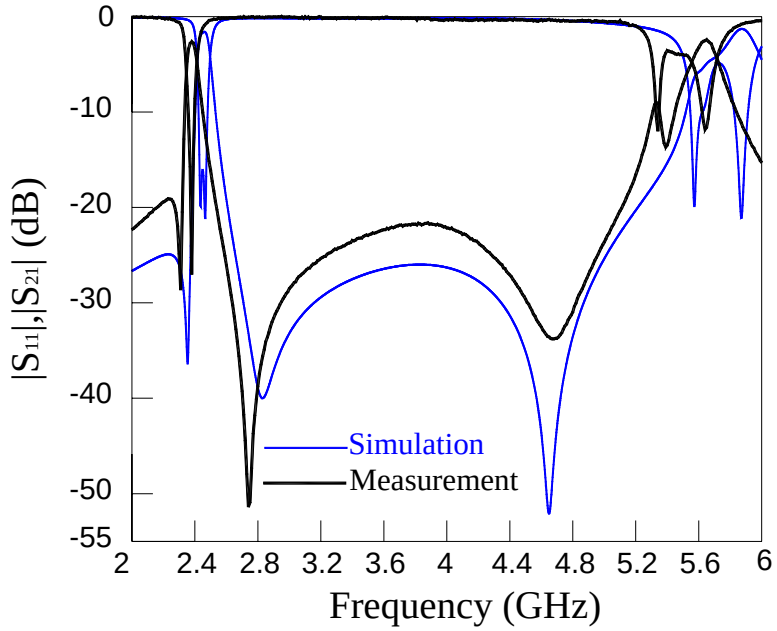

(b)

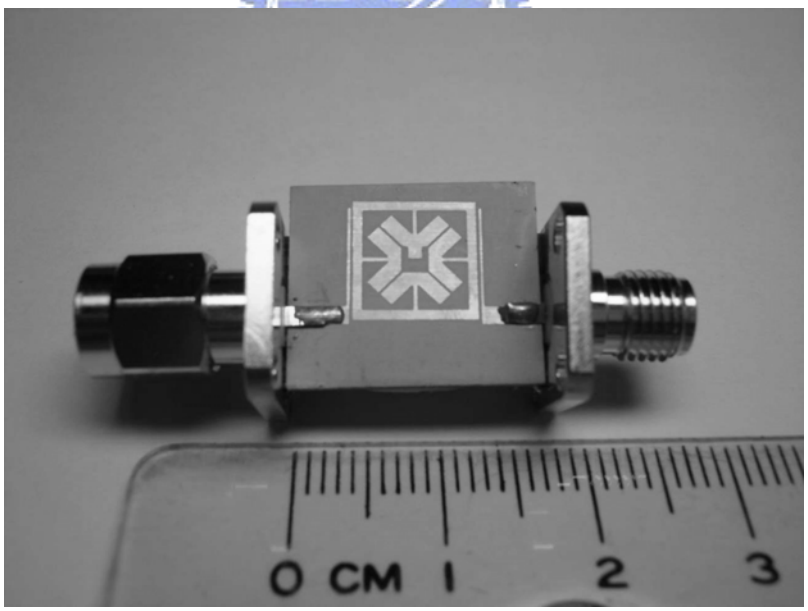

(c)

Figure 2-13 Simulated and measured filter responses for R=0.62 in (a) a narrow band, (b) broadband and (c) circuit photo.

Chapter 3

Periodic Stepped-Impedance Ring Resonator (PSIRR) Bandpass Filter with a Miniaturized Area and Desirable Upper Stopband Characteristics

A periodic stepped-impedance ring resonator (PSIRR) is proposed to design dual-mode bandpass filters with a miniaturized area. Design parameters of a PSIRR include impedance ratio *R* of the hi-*Z* to low-*Z* sections, their lengths, and number of impedance steps 2*N*. The resonant characteristics of PSIRRs with various *N* and *R* values are investigated by both the transmission line theory and EM simulation. Proper choice of above parameters leads to an optimal reduction of circuit area and extension of upper rejection bandwidth. Realized by the standard fully planar microstrip technology, the proposed dual-mode PSIRR bandpass filter has not only the first spurious response at higher than 3.7 times the passband frequency but also an area reduction of better than 60% against a conventional ring filter. Two transmission zeros exist in the upper stopband and are tunable via changing the arm lengths of the line-to-ring coupling structure. Measurement results of several fabricated circuits validate the analysis and theoretical prediction.

3.1 The Periodic Stepped-Impedance Ring Resonator

Figure 3-1 shows layouts of the proposed PSIRRs of N = 1 through 4. Each PSIRR consists of N hi-Z sections of a spatial angle $2\theta_1$. Every two adjacent hi-Z sections are spaced by a low-Z section of a spatial angle $2\theta_2$. All PSIRRs are symmetric about at least one dashed line so that $\theta_1 + \theta_2 = \pi/N$. Such a PSIRR is called PSIRRN herein. For example, a PSIRR with N = 3 is denoted as PSIRR3. For the PSIRR1 and PSIRR2, the Z_2-sections are perturbations of the ring. When $N \geq 3$ the Z_3-section is a perturbation of the Z_2-section to split off the degenerate modes. For circuit analysis, define the impedance ratios of a PSIRR as

$$R = \frac{Z_1}{Z_2} \geq 1 \tag{3.1a}$$

$$R' = \frac{Z_1}{Z_3} \geq 1 \tag{3.1b}$$

where R'/R is close to unity and R' is used only for $N \geq 3$.

The resonant conditions for the PSIRRs can be formulated by the transmission line theory [4]. First, taking PSIRR2 for instance, the two resonance modes within the ring resonator are indicated as odd and even modes shown in Figure 3-2. The resonant conditions can be determined by enforcing the respective input admittances to zero:

$$\begin{aligned} Y_{in}^{e} &= 0 \\ Y_{in}^{o} &= 0 \end{aligned} \tag{3.2}$$

Therefore, the resonant frequencies f_{even} and f_{odd} can be calculated.

Even Mode:

$$\tan 2\theta_1^e + 2R\ \tan\theta_2^e - R^2 \tan 2\theta_1^e \tan^2\theta_2^e = 0 \tag{3.3a}$$

where

$$\theta_1^e = \frac{\theta_1 f_{even}}{f_0}, \theta_2^e = \frac{\theta_2 f_{even}}{f_0}, \theta_1 + \theta_2 = \frac{\pi}{2}$$

Odd Mode:

$$R^2 \tan 2\theta_1^o + 2R\ \tan\theta_2^o - \tan 2\theta_1^o \tan^2\theta_2^o = 0 \tag{3.3b}$$

where

$$\theta_1^o = \frac{\theta_1 f_{odd}}{f_0}, \theta_2^o = \frac{\theta_2 f_{odd}}{f_0}, \theta_1 + \theta_2 = \frac{\pi}{2}$$

θ_1^e (θ_1^o) and θ_2^e (θ_1^o) are electrical lengths of spatial angles θ_1 and θ_2, respectively, and f_0 is the resonant frequency of a uniform ring resonator.

The next example is the PSIRR3. The PSIRR3 can be modeled by the multistepped-impedance lines with terminations Z_L shown in Figure 3-3. The odd and even resonances of the PSIRR3 occur when Z_L = 0 and ∞, respectively. For the odd mode, the resonant condition can be formulated by letting the input admittance to zero as follows

$$Z_{left} = jZ_1 \frac{Z_3 \tan\theta_2^o + Z_1 \tan 2\theta_1^o}{Z_1 - Z_3 \tan 2\theta_1^o \tan\theta_2^o} \tag{3.4a}$$

$$Z_{right} = jZ_2 \frac{Z_1 \tan\theta_1^o + Z_2 \tan 2\theta_2^o}{Z_2 - Z_1 \tan\theta_1^o \tan 2\theta_2^o} \tag{3.4b}$$

At resonance,

$$Y_{odd} = \frac{1}{Z_{odd}} = \frac{1}{Z_{left}} + \frac{1}{Z_{right}} = 0 \tag{3.5}$$

where Z_{right} and Z_{left} are the input impedances seen at the Z_1-Z_2 junction looking to the right and left. Substituting equations (3.4a) and (3.4b) into (3.5), we have

$$\frac{1}{Z_1}\frac{Z_3 \tan 2\theta_1^o \tan\theta_2^o - Z_1}{Z_3 \tan\theta_2^o + Z_1 \tan 2\theta_1^o} + \frac{1}{Z_2}\frac{Z_1 \tan\theta_1^o \tan 2\theta_2^o - Z_2}{Z_1 \tan\theta_1^o + Z_2 \tan 2\theta_2^o} = 0 \tag{3.6}$$

where θ_1^o and θ_2^o are electrical lengths of spatial angles θ_1 and θ_2, respectively. Rearranging (3.6), we obtain the resonant condition of the odd-mode resonance:

$$\begin{aligned} &\tan 2\theta_1^o \tan\theta_2^o (R\tan\theta_1^o + \tan 2\theta_2^o) + R^2 \tan\theta_1^o \tan 2\theta_2^o (\tan\theta_2^o + R' \tan 2\theta_1^o) \\ &- R' \tan 2\theta_2^o - R\tan\theta_2^o - R'R\ (\tan 2\theta_1^o + \tan\theta_1^o) = 0 \end{aligned} \tag{3.7}$$

Based on (3.3) and (3.7), a simple root-searching program can be employed to calculate the resonant frequencies. It can be anticipated that the frequencies can be easily tuned by changing values of R, R', θ_1, and θ_2. The above even- and odd-mode analysis is also applied to alle other PSIRRs. Note that the above discussion assumes the TEM mode and ignores step discontinuities along the ring. Figure 3-4 plots the leading two resonant frequencies for PSIRRs with N = 1, 2, …, 8 against θ_2 from 0 to min($\pi/2$, π/N) for R = 4 and R' = 1.04×R. The plotted frequencies are normalized with respect to the fundamental frequency of a uniform impedance ring resonator (UIRR) f_0, i.e., Z_1 = Z_2 = Z_3. Here, all the PSIRRs have identical mean radii. When circuit

miniaturization is the design target, the desired resonator will have a frequency as low as possible. As indicated in Figure 3-4, PSIRR2 has the lowest resonant frequency. Its second resonance, however, is far away from the previous one due to the large R value. Note that the design frequency of a dual-mode ring filter should be the algebraic mean of these two resonances, i.e., $(f_a + f_b) / 2$. Obviously, the mean will not be the lowest resonant frequency if N and θ_2 are free to change. In addition, the large distance between the two resonances will lead to a filter with a large bandwidth, but at the same time impractically large couplings between feeders and the ring can be inevitable.

3.2 Resonator Miniaturization and the Upper Stopband

For PSIRRs with $N \geq 3$, as indicated in Figure 3-4, the two resonant frequencies, f_a and f_b, have a small distance in response to the 4% change of Z_2 to Z_3. Assume that both f_a and f_b originate from f_1, the degenerate frequency, and that $f_a > f_b$. In the plotted range of θ_2, each PSIRR has a minimal resonant frequency. In our theoretical calculation, one of the degenerate frequency f_a is nearly unchanged due to the perturbation, i.e., $f_a \approx f_1$. Detailed data show that the minimal resonant frequencies locate at $\theta_1 = \theta_2 = \pi/2N$. The normalized frequencies f_a and f_b can be further lowered if the impedance ratio R is increased.

When $R = 4$, the minimal normalized f_a values for N from 3 through 8 are listed in Table I. In the table, the f_a value for $N = 4$ is about 4.8% higher than that for $N = 3$. It implies that when they are designed at the same frequency, the former will occupy a resonator area of 9.8% more than the latter. The minimal normalized resonant frequencies for $3 \leq N \leq 8$ are between 0.7 and 0.8. Note that the area reduction depends also on R value. Table II lists the minimal f_a of PSIRR3 and PSIRR4 when $2.5 \leq R \leq 5$. As compared with a UIR resonator, the PSIRR3 with $R = 4.5$ will use

only $(0.6958)^2$ = 48.4% area. An area reduction of 51.6% can be achieved. The simulation and measured results shown below indicate that a further reduction can be obtained due to certain parasitic effects, for example, the large discontinuity junction. This point will be addressed soon.

TABLE I

MINIMAL NORMALIZED RESONANT FREQUENCIES FOR PSIRRS WITH $R = 4$

N	3	4	5	6	7	8
f_a	0.7316	0.7666	0.7801	0.7868	0.7910	0.7933

TABLE II

MINIMAL NORMALIZED FREQUENCIES f_a FOR PSIRR3 AND PSIRR4

R	2.5	3	3.5	4	4.5	5
$N = 3$	0.8511	0.8098	0.7677	0.7316	0.6958	0.6700
$N = 4$	0.8825	0.8392	0.8003	0.7666	0.7346	0.7069

It is also desirable for a distributed bandpass filter to have a wide upper stopband. The performance of the filter in the upper stopband depends much on where the first higher-order resonance f_2 arises. Figure 3-5 depicts the fundamental and first harmonic resonant frequencies against θ_2 for R = 3, 4, and 4.5 for PSIRR3. Figure 3-6 plots f_2/f_1 against θ_2 for R = 3, 4, and 4.5 for PSIRR3 and PSIRR4. As indicated, the θ_2 where maximal f_2/f_1 occurs at coincides with that minimal f_1 does. It means that choosing $\theta_1 = \theta_2$ for a PSIRR structure will have at the same time a minimal ring area and maximally possible upper stopband.

Figure 3-7 compares the resonant spectrum of a PSIRR3 and a PSIRR4 for $R = 4.5$ with that of a UIR resonator on a dielectric substrate with $\varepsilon_r = 10.2$ and thickness = 1.27 mm. All rings have identical mean radii r' = 6.27 mm. This size will be used for all the PSIRR filters herein. It can be easily verified that the UIR has f_1 = 3 GHz. The

simulation data are obtained by the EM software package IE3D [14]. The fundamental resonances of the PSIRR3 and PSIRR4 are at 1.93 and 1.98 GHz, respectively. Thus, the minimal normalized frequencies f_1 for both cases are 0.643 and 0.660. These two values are about 10% less than those given in Table II. This should be resulted from the parasitic effects in the $2N$ step discontinuities along the ring. In other words, for the particular PSIRR structures, more area reduction can be expected from the full-wave simulation data than that from the theoretic prediction by the transmission line theory.

For the particular I/O arrangement, the first higher-order resonance of the UIR is at $2f_1$ = 6 GHz, while those of the PSIRR3 and PSIRR4 are at 6.04 and 7.35 GHz, respectively. The corresponding ratios of f_2/f_1 of PSIRR3 and PSIRR4 are 3.13 and 3.71. These two values are about 5% less than those shown in Figure 3-6. For the PSIRR4, if the I/O feeds are taken collinearly passing through the low-Z sections, there is a higher-order resonance at 2.9 GHz and the resonance at 7.35 GHz disappears at the same time.

3.3 Dual-Mode Ring Filter Design

For a dual-mode ring resonator bandpass filter, the feeders should be properly designed such that a symmetric passband response can be obtained. Figure 3-8 plots the $|S_{21}|$ response for a PISRR3 having R = 4.2 and R' = 4.6 with various separations θ between the feeders, which is symmetric about a vertical axis through center of the ring and has a small gap to the ring. It is found that there are two possible separations, $\theta = 60^o$ and 255^o to make the $|S_{21}|$ response have equal peaks at f_a and f_b. For a PSIRR4, simulation is done with the Z_3-section being symmetrically located at vertical axis above the center of the ring. Figure 3-9 plots the $|S_{21}|$ response for a PISRR4 having R = 4.5 and R' = 5.15 with various separations θ between the feeders,

which have same orientation as the feeders used in PSIRR3.

The purpose that *R'* is made a little bit larger than *R* is to produce a proper coupling between the two degenerate modes. This perturbation is similar to the conventional patch perturbation in [4, 7-9, 11]. The coupling coefficient between the two modes in a PSIRR can be calculated by (2.8). Note that f_a and f_b are consistent with those used in Figure 3-4.

As indicated in Figure 3-8 (c), the peak $|S_{21}|$ levels for $\theta = 60^o$ is about 7 dB higher than that for $\theta = 255^o$. It means that the latter will need more I/O couplings than the former for the synthesis of a given filter bandwidth. However, the I/O search for PSIRR4 as indicated in Figure 3-9 (c), the peak $|S_{21}|$ levels for $\theta = 90^o$ is almost the same as that for $\theta = 275^o$. It can be anticipated that both of the I/O separations will result in same passband response for the same I/O couplings. To establish the necessary couplings between the dual-mode resonator and the feeders, the line-to-ring strong coupling structures [6] is used herein.

Both the PSIRR3 and PSIRR4 filters are found to have two zeros in the upper stopband before the first spurious arises. These zeros are desirable since they greatly improve the rejection levels in the stopband. For investigating the properties of these two zeros, Figures 3-10 (a) and 3-10 (b) plot the simulation responses of the PSIRR3 and PSIRR4 filters, where the feeders have total arc lengths $\phi_1 + \phi_2 = 140^o$ and 108^o, respectively. Here, $R = 4.13$ and $R' = 4.57$. The coupling arms have a width and a gap from the ring of 0.14 mm. In Figure 3-10(a), when ϕ_1 is decreased from 40^o to 25^o, the distance between the two zeros increases. The separation between the I/O ports is kept constant during the change of ϕ_1. Note that the passband responses are close to being not altered. The results in Figures 3-10(a) and 3-10(b) indicate that the two zeros are tunable via adjusting ϕ_1.

The even and odd analysis [2] can be invoked to predict the two extra zeros for the

PSIRR1 circuits. The analysis network for the prediction includes coupled line sections loaded with short-circuited or open stubs. Such an analysis for PSIRR3 and PSIRR4, however, will be tedious. Nevertheless, mechanism for generation of the two zeros in Fig. 7 is now clear and believed to be the same as the PSIRR1 case.

3.4 Simulations and Measurements

Four dual-mode PSIRR bandpass filters are fabricated on a substrate with ε_r = 10.2 and thickness = 1.27 mm. All the rings have a radius r = 6.2 mm. The relative structure parameters are listed in Table III. Figures 3-11 and 3-12 show the layout, simulation and measured results for two PSIRR4 filters, with I/O port separations θ = 90° and 275°, respectively. Both of them have a center frequency f_o = 1.93 GHz. In Figure 3-11, the measured bandwidth Δ = 6.25 %. Figure 3-11 (a) shows the layout of the PSIRR4 bandpass filter. The local and broadband responses are shown in Figure 3-11 (b) and (c), respectively. Figure 3-11 (d) is the photo of the fabricated circuit. In Figure 3-12, the PSIRR4 is a duplicate of the previous one with Z_3 = 19.88 Ω for reducing the bandwidth to 4.5%. The circuit feeders have ϕ_1 = 90° and ϕ_2 = 10° so that the two zeros have a larger separation than that in Figure 3-11 (c). Figure 3-12 (a) and (c) show the layout and photo of the circuit. Both filters in Figure 3-11 and 3-12 have in-band insertion losses of 1.7 dB and return losses close to 20 dB. Note that these two circuits use only $(1.93/3)^2$ = 41.4% of the area of a regular dual-mode ring resonator filter. In 3 ~ 4 GHz band, the $|S_{21}|$ in Figure 3-11 (c) shows better filter performance in the upper stopband than that in Figure 3-12 (b). The situation is reversed if 4.5 ~ 5.5 GHz band is concerned. The spurious responses of the two circuits have peaks at 7.3 GHz or 3.78f_o, as well predicted by Figure 3-7.

Figure 3-13 (b) plots the simulation and measured results of a PSIRR3 filter, whose Z_1 and Z_2 are identical to those used in Figure 3-11, but Z_3 = 19.18 Ω. The

separation between the input and output ports θ = 60°, and lengths of the feeders' arms ϕ_1 = 17° and ϕ_2 = 93° as shown in Figure 3-13 (a). In measurement, passband center f_o = 1.85 GHz, Δ = 8%, and in-band insertion loss is 1.24 dB. The circuit occupies only 38% of the area of a regular dual-mode UIR filter at the same design frequency. The peak of spurious response is detected at 6 GHz or 3.24f_o. Figure 3-13 (d) shows the photo of the circuit in Figure 3-13 (b).

Figure 3-13 (c) plots the simulation and measured responses of the second PSIRR3 filter. The circuit is a duplicate of that in Figure 3-13 (b) with Z_3 being changed to 19.88 Ω. With ϕ_1 = 17°, the distance ϕ_2 is swept from 100° to 70° to tune the notch at 5 GHz in Figure 3-13(b). Simulated $|S_{21}|$ responses with ϕ_2 = 98.3°, 85.8°, 75.1°, and 71.5° are plotted to show the migration of the notch. When ϕ_2 = 71.5°, the notch cancels the spurious response at 6 GHz so that the upper stopband has 1 GHz bandwidth extension for a 20-dB rejection level. This circuit is fabricated as shown in Figure 3-13 (e) and measured. The measured insertion loss in the passband is only 1.6 dB. As can be seen from the plots, the measured responses have good agreement with the simulation.

TABLE III

THE DETAIL CIRCUIT DIMENSIONS FOR THE FILTER IN FIGURE 3-11~3-13

Filter	ϕ_1 (°)	ϕ_2 (°)	r (mm)	W_1 (mm)	W_2 (mm)	W_3 (mm)	L_1 (mm)	L_2 (mm)	L_3 (mm)	d (mm)	Z_1 (Ω)	Z_2 (Ω)	Z_3 (Ω)
Figure 3-11	30	80	6.2	0.14	4.4	5.45	5.42	4.53	4.53	0.14	102.5	22.78	19.47
Figure 3-12	10	90	6.2	0.14	4.4	5.3	5.42	4.53	4.53	0.14	102.5	22.78	19.88
Figure 3-13(b)	17	93	6.2	0.14	4.4	5.56	7.32	5.95	5.95	0.14	102.5	22.78	19.18
Figure 3-13(c)	17	73	6.2	0.14	4.4	5.3	7.32	5.95	5.95	0.14	102.5	22.78	19.88

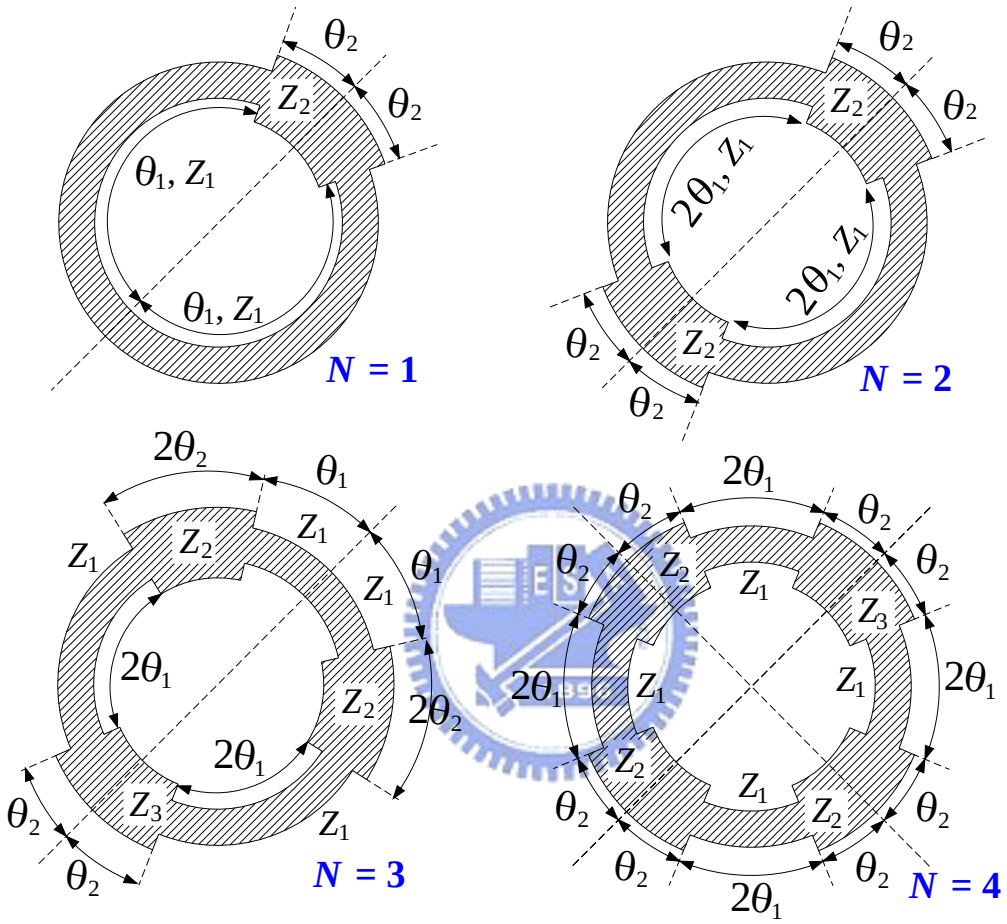

Figure 3-1 Layouts of the proposed PSIRRs for N = 1, 2, 3, and 4. $\theta_1 + \theta_2 = \pi/N$.

PSIRR2

Even Mode

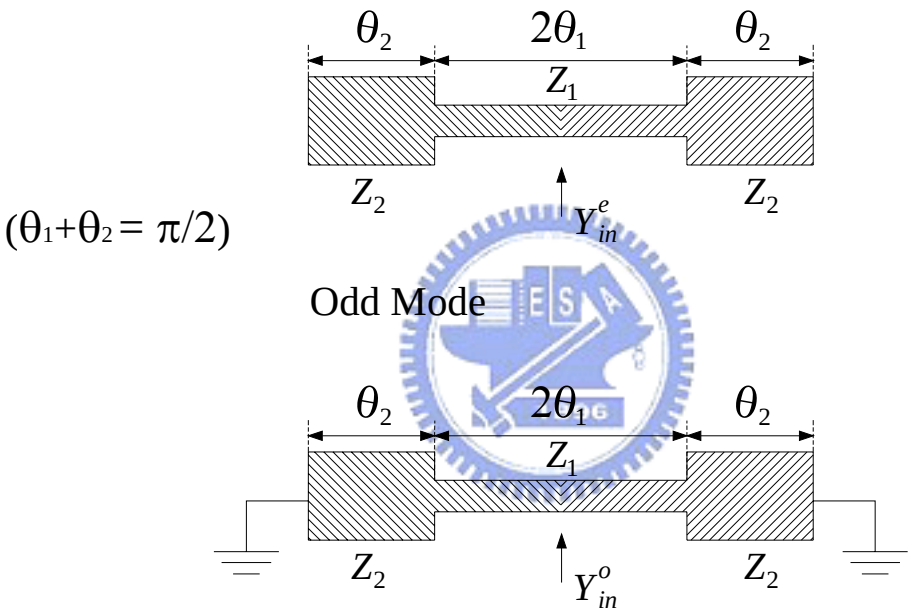

Figure 3-2 The odd and even modes transmission line modeling of a PSIRR2.

PSIRR3

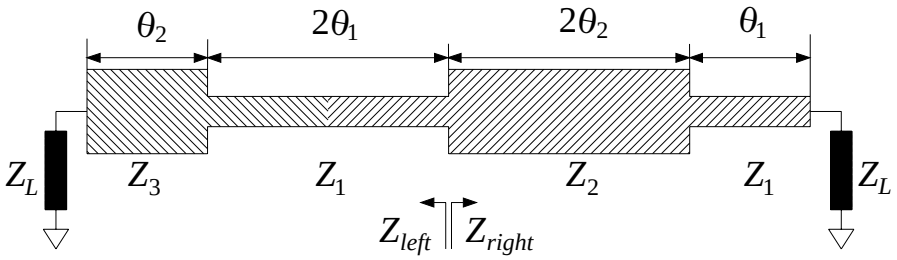

Figure 3-3 Transmission line modeling of a PSIRR3. In analysis, Z_L = 0 and ∞ for the odd and even modes, respectively.

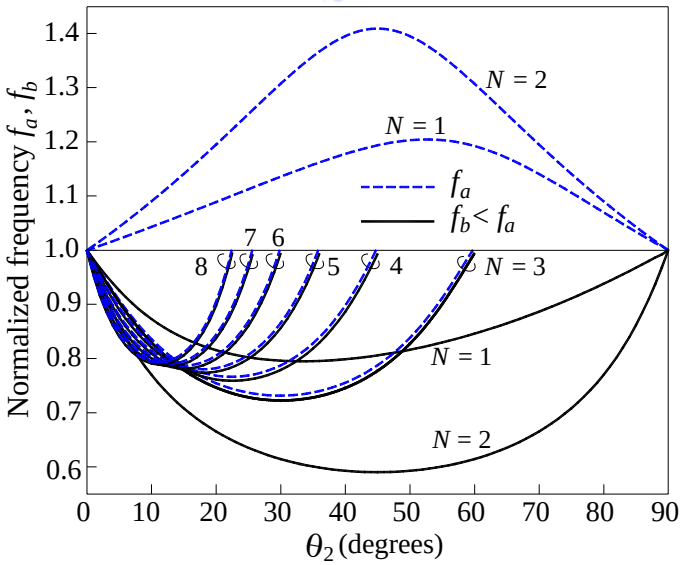

Figure 3-4 Normalized resonant frequencies of perturbed PSIRRs for N = 1, 2, …, 8. All rings have identical radii.

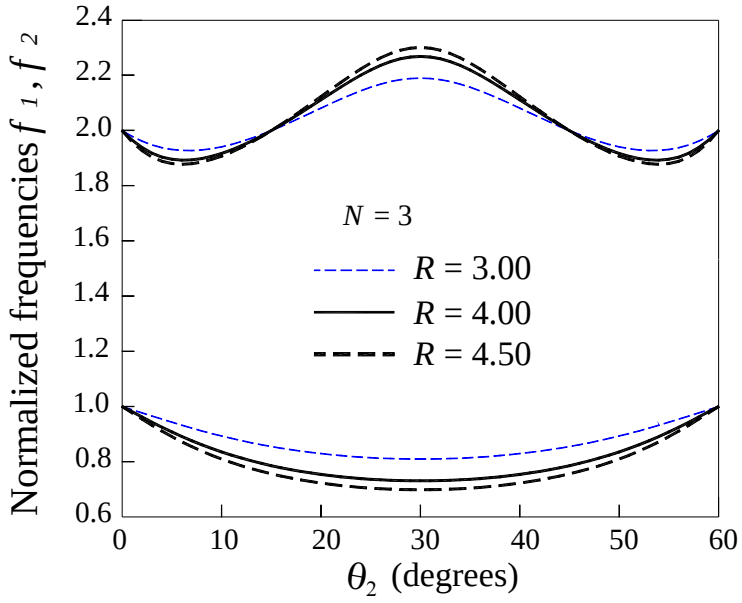

Figure 3-5 The fundamental resonant frequency and the first higher-order resonance for PSIRRs with N = 3.

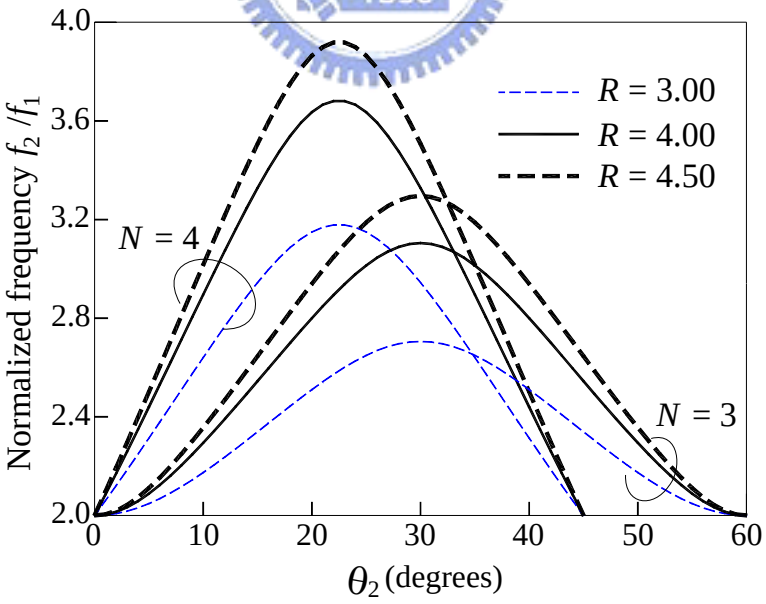

Figure 3-6 Ratios of the first higher-order resonant frequency to the fundamental resonance for PSIRRs with N = 3 and 4.

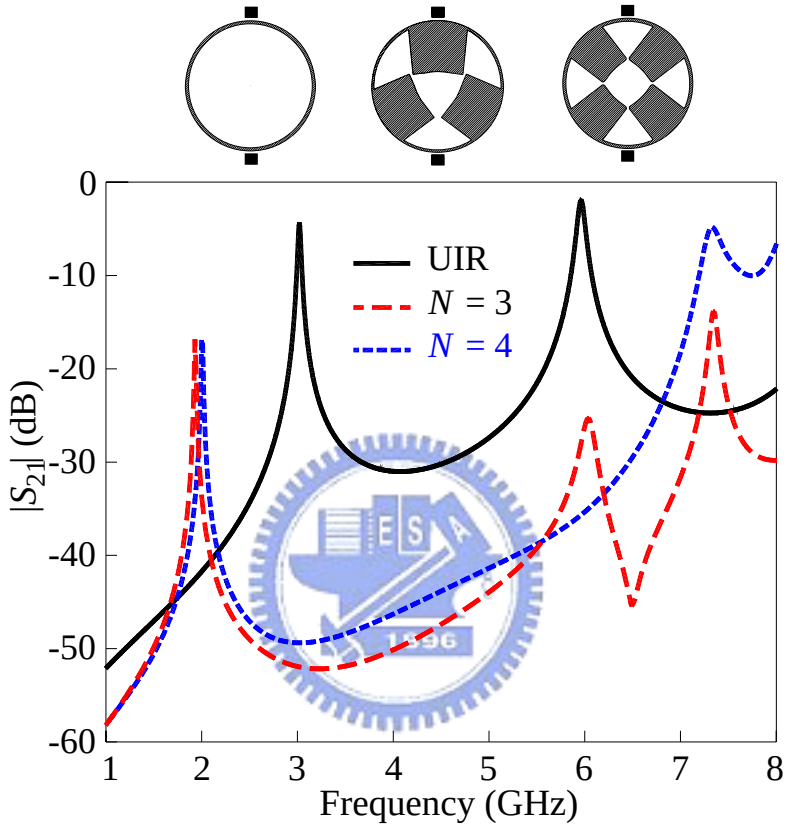

Figure 3-7 Normalized fundamental and first higher-order resonant frequencies of the PSIRR3 and PSIRR4.

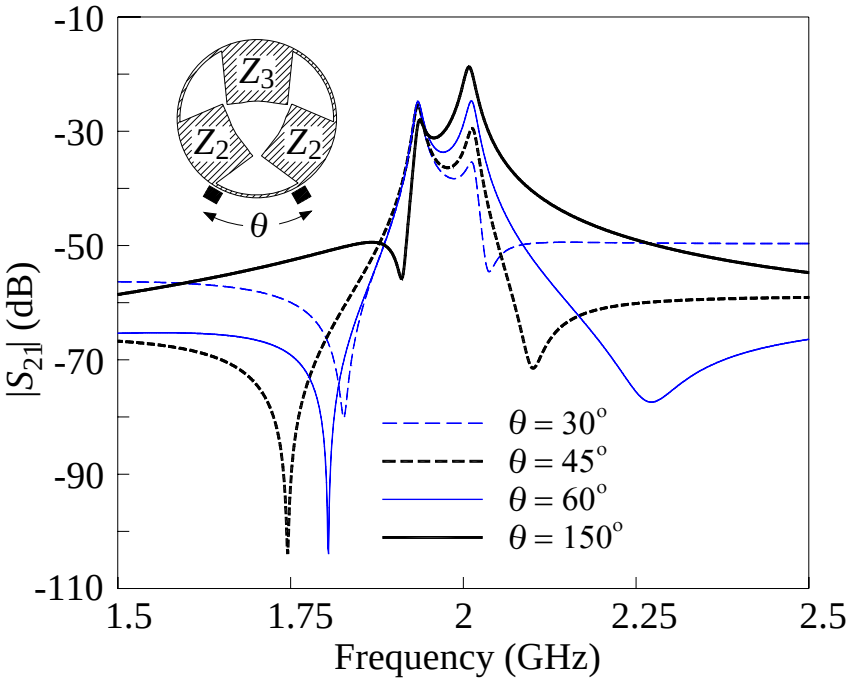
-10
-30
-50
-70
-90
-110
1.5
1.75
2
2.25
2.5
Frequency (GHz)
|S21| (dB)
Z3
Z2
Z2
θ
θ = 30°
θ = 45°
θ = 60°
θ = 150°

(a)

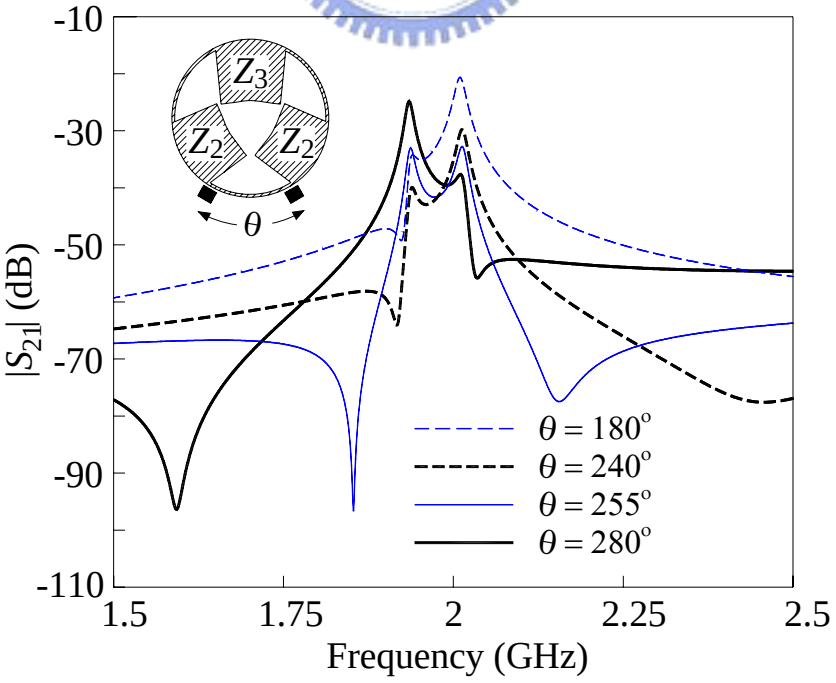
-10
-30
-50
-70
-90
-110
1.5
1.75
2
2.25
2.5
Frequency (GHz)
|S21| (dB)
Z3
Z2
Z2
θ
θ = 180°
θ = 240°
θ = 255°
θ = 280°

(b)

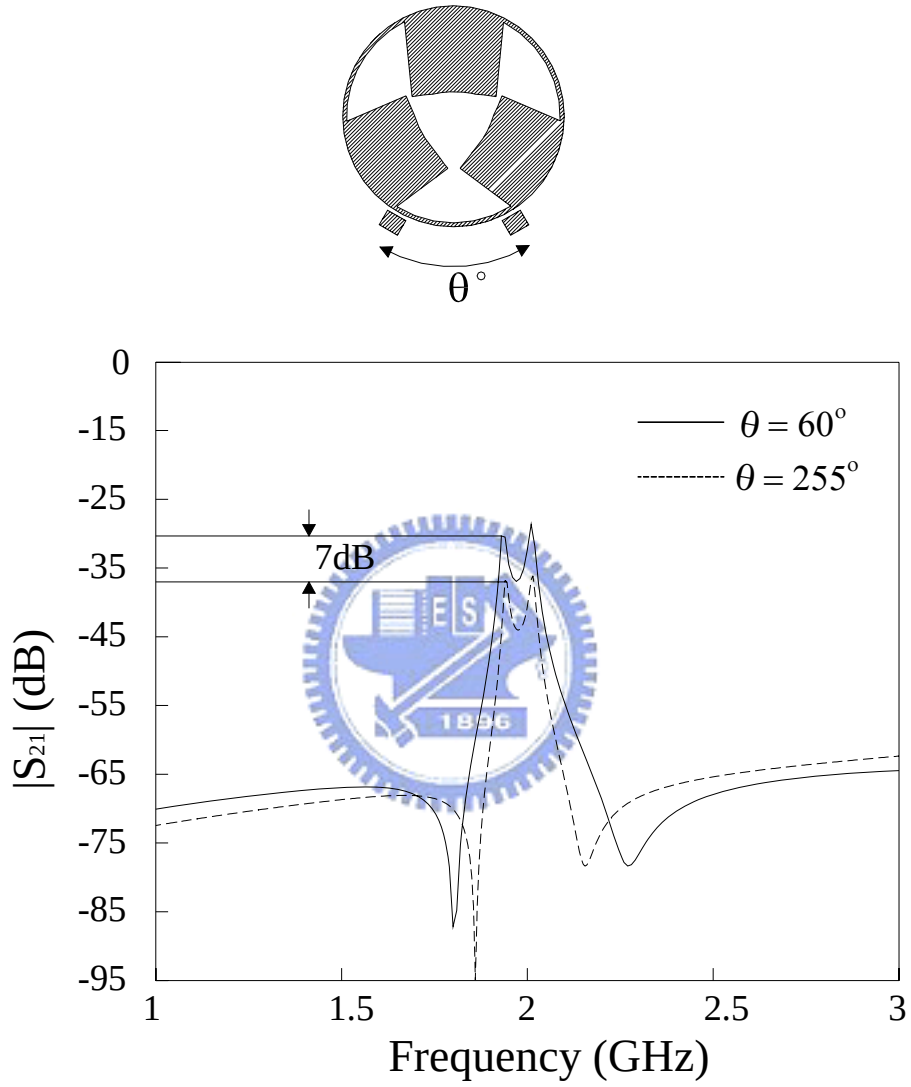

(c)

Figure 3-8 Search for spatial separation θ between I/O feeders for a PSIRR3. (a) θ = 30°, 45°, 60°, 150°. (b) θ = 180°, 240°, 255°, 280°. (c) θ = 60°, 255°.

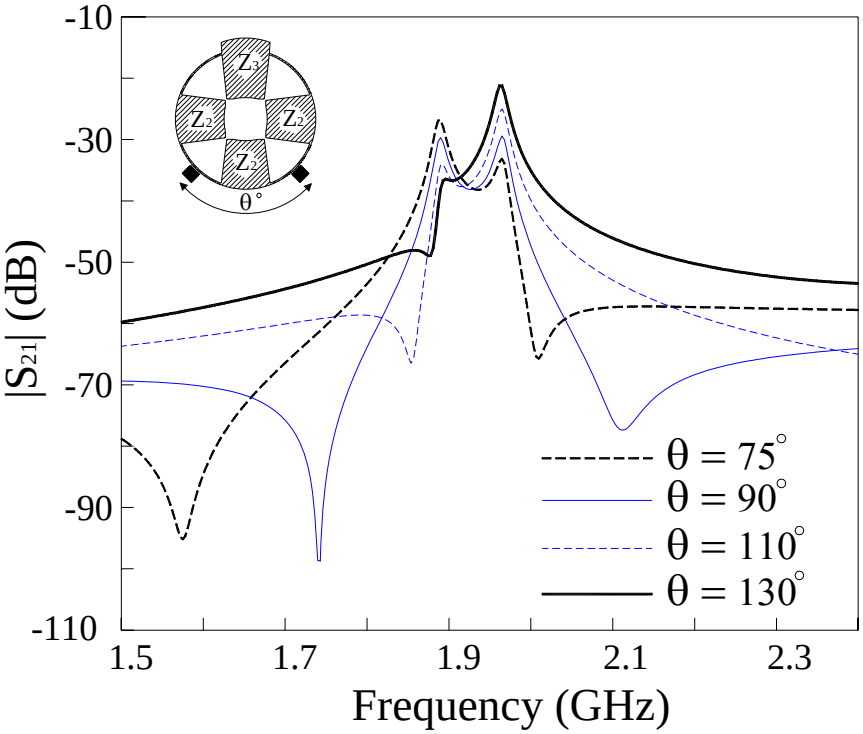
-10
-30
-50
-70
-90
-110
|S21| (dB)
1.5
1.7
1.9
2.1
2.3
Frequency (GHz)
Z3
Z2
Z2
Z2
θ°
θ = 75°
θ = 90°
θ = 110°
θ = 130°

(a)

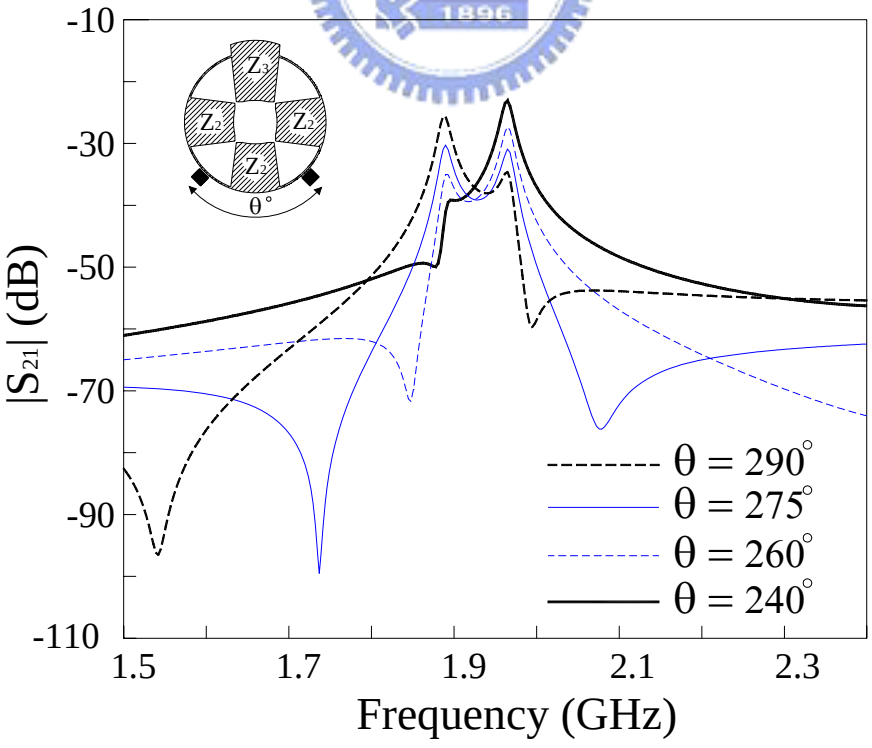
-10
-30
-50
-70
-90
-110
|S21| (dB)
1.5
1.7
1.9
2.1
2.3
Frequency (GHz)
Z3
Z2
Z2
Z2
θ°
θ = 290°
θ = 275°
θ = 260°
θ = 240°

(b)

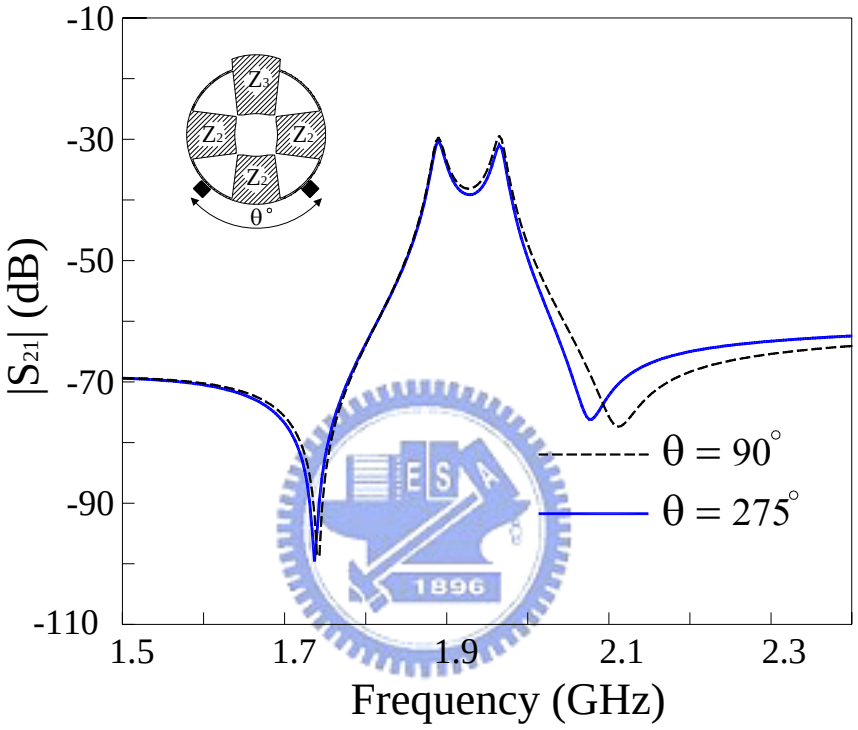

(c)

Figure 3-9 Search for spatial separation θ between I/O feeders for a PSIRR4. (a) θ = 75°, 90°, 110°, 130°. (b) θ = 240°, 260°, 275°, 290°. (c) θ = 90°, 275°.

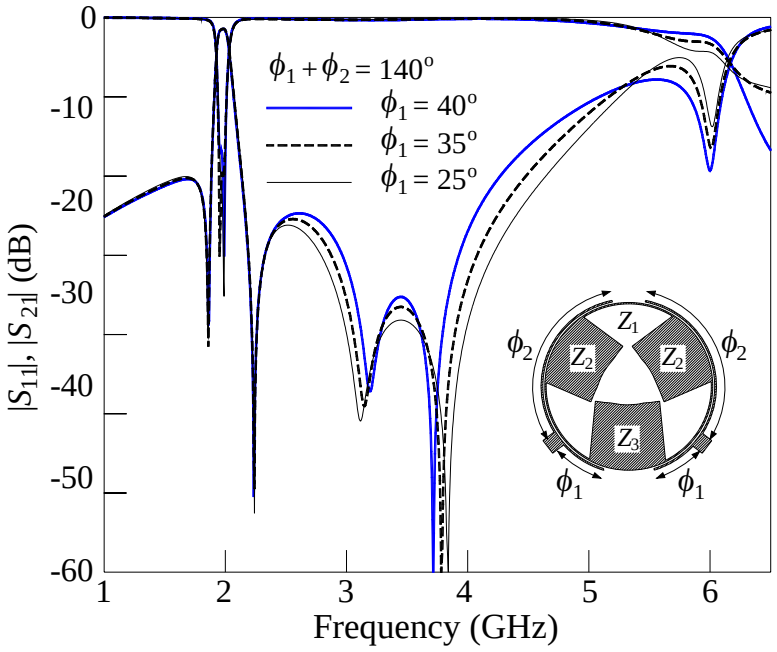

(a)

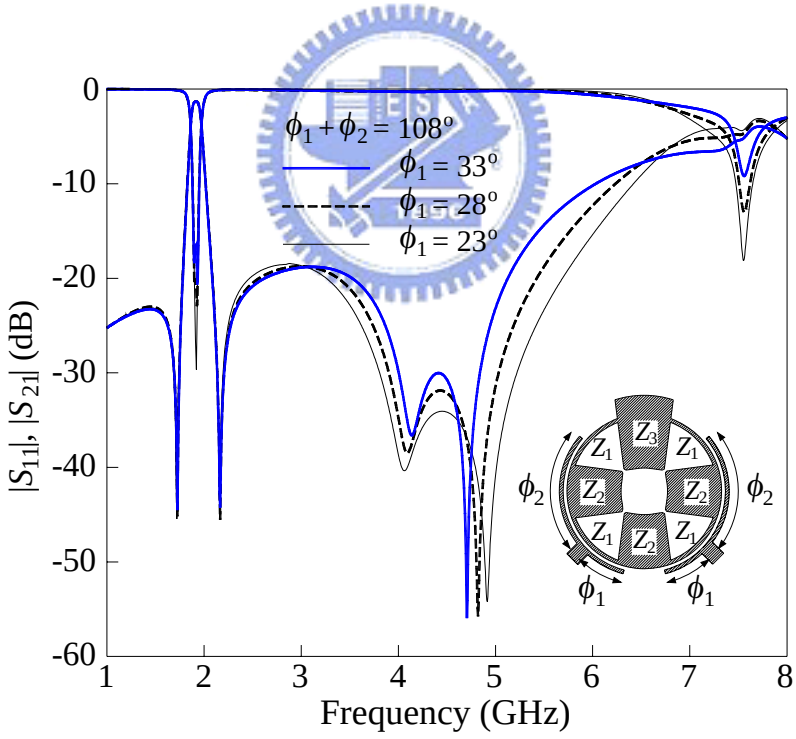

(b)

Figure 3-10 Tuning of the two transmission zeros in the upper stopband for two PSIRR filters. (a) N = 3. (b) N = 4.

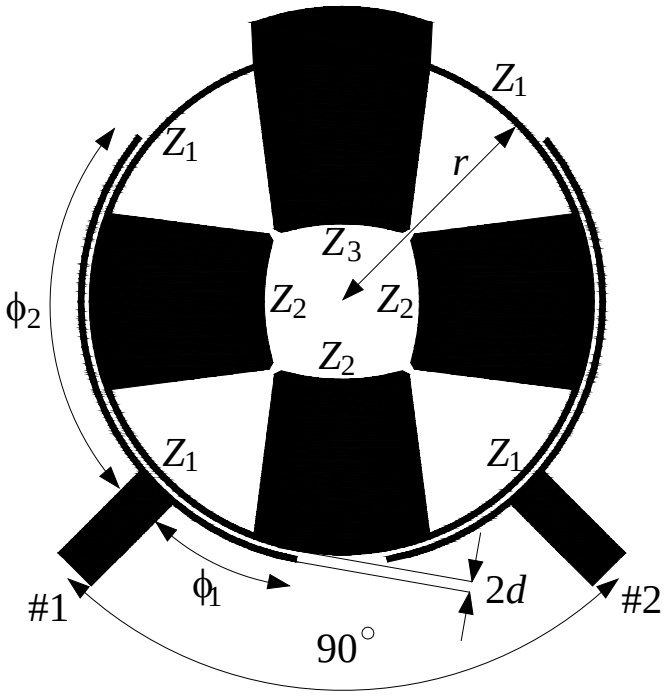
Z1
Z1
r
Z3
Z2
Z2
Z2
ϕ2
Z1
Z1
ϕ1
2d
#1
#2
90°

(a)

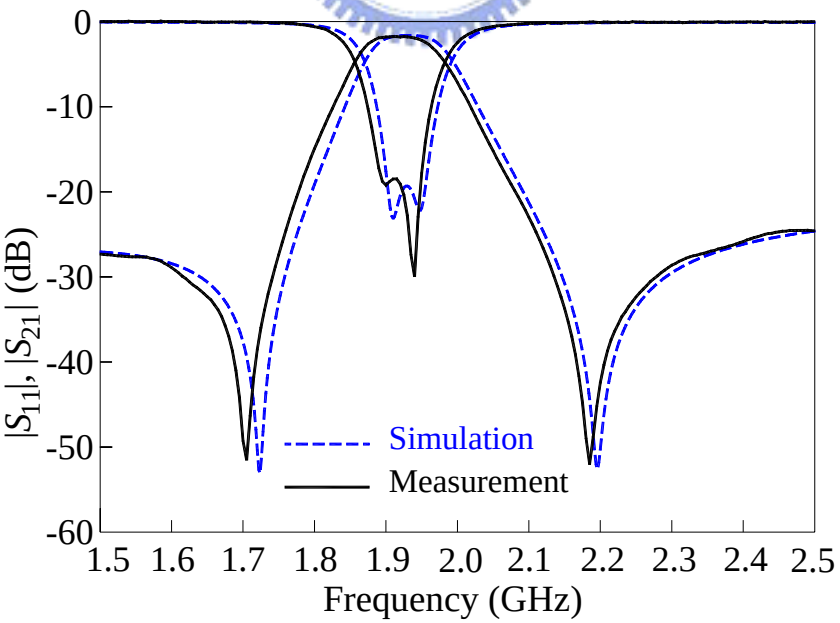
0
-10
-20
-30
-40
-50
-60
|S11|, |S21| (dB)
Simulation
Measurement
1.5
1.6
1.7
1.8
1.9
2.0
2.1
2.2
2.3
2.4
2.5
Frequency (GHz)

(b)

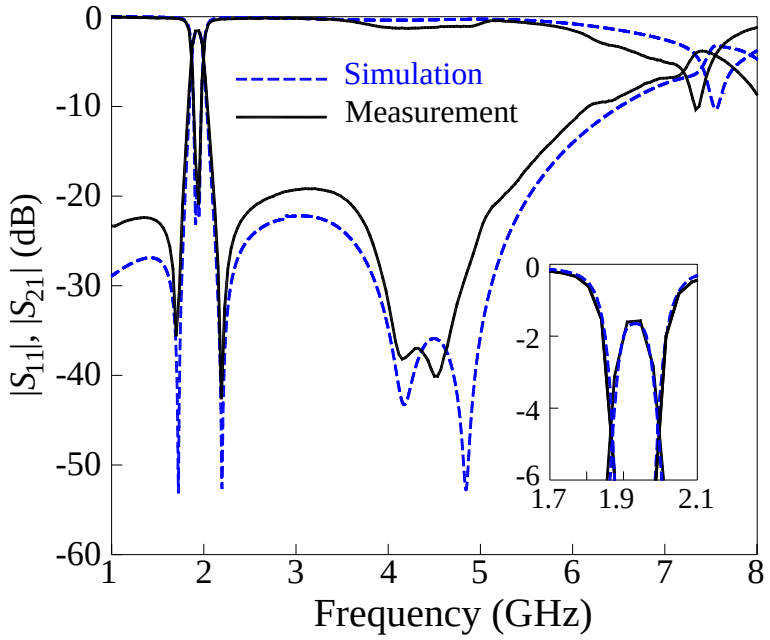

(c)

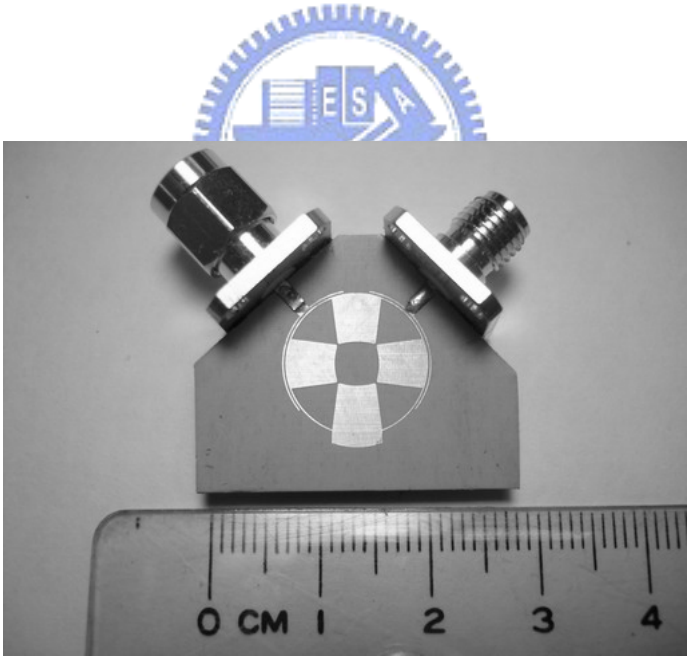

(d)

Figure 3-11 The dual-mode bandpass filter of PSIRR4. R = 4.5, R' = 5.3, θ = 90°, ϕ_1 = 30°, ϕ_2 = 80°.(a) Layout. (b) Local simulation and measurement results. (c) Simulation and measurement results in the broadband. (d) Photo of the circuit. Substrate: ε_r = 10.2, thickness = 1.27 mm.

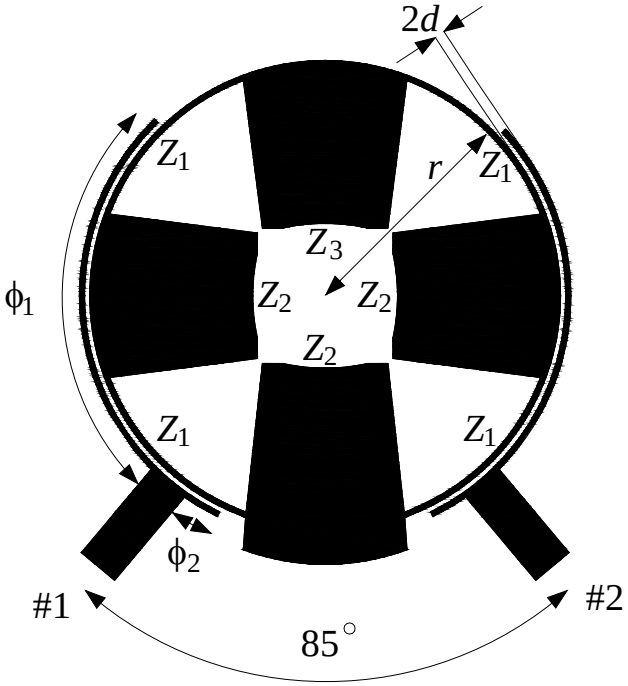
2d
Z1
r
Z1
Z3
ϕ1
Z2
Z2
Z2
Z1
Z1
ϕ2
#1
#2
85°

(a)

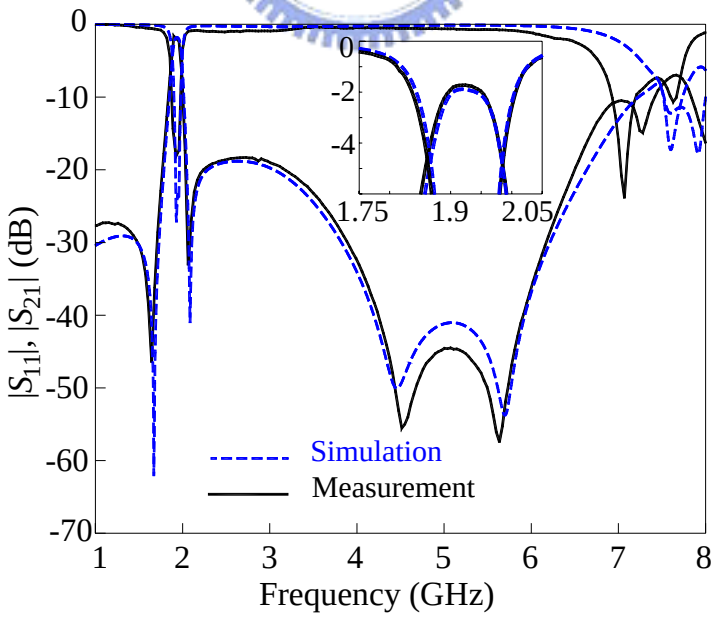
0
-10
-20
-30
-40
-50
-60
-70
|S11|, |S21| (dB)
1
2
3
4
5
6
7
8
Frequency (GHz)
Simulation
Measurement
0
-2
-4
1.75
1.9
2.05

(b)

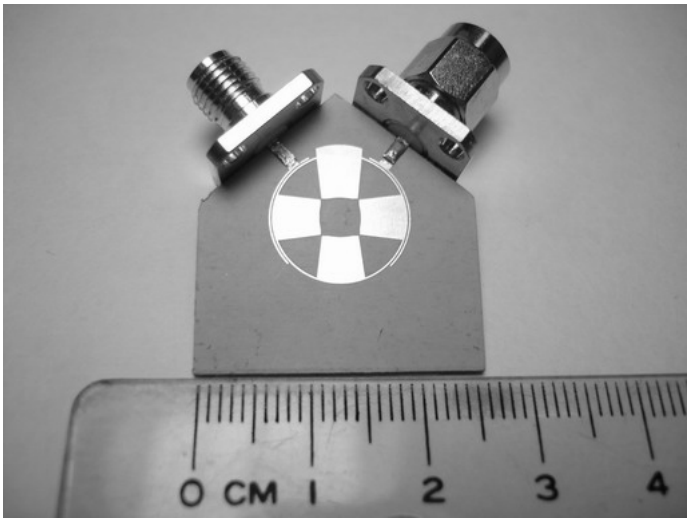

(c)

Figure 3-12 The dual-mode bandpass filter of PSIRR4. R = 4.5, R' = 5.15, θ = 275°, ϕ_1 = 90°, ϕ_2 = 10°(a) Layout. (b) Simulation and measurement results. (c) Photo of the circuit. Substrate: ε_r = 10.2, thickness = 1.27 mm.

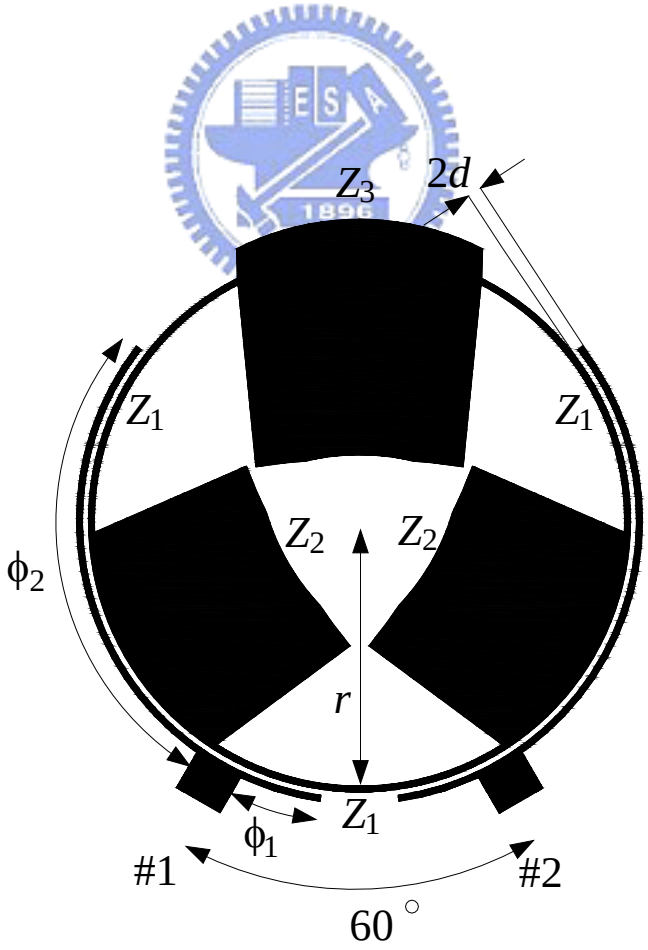

(a)

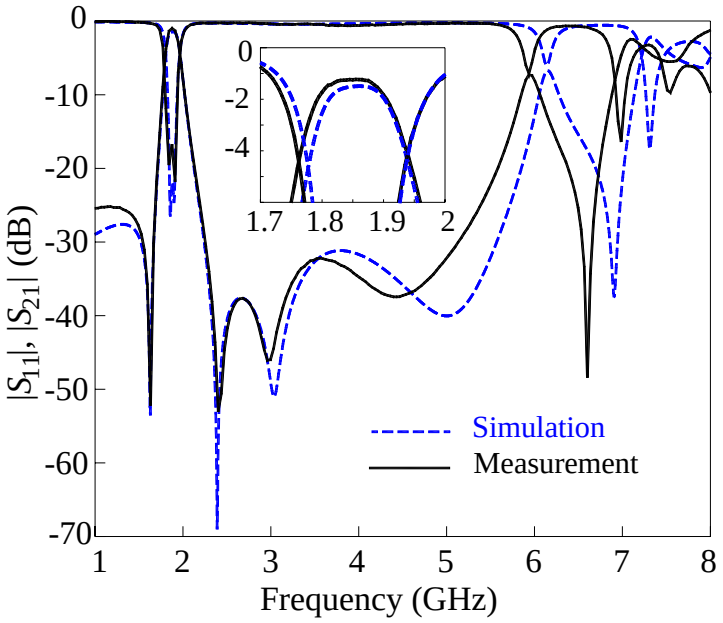
0
-10
-20
-30
-40
-50
-60
-70
1
2
3
4
5
6
7
8
Frequency (GHz)
|S11|, |S21| (dB)
Simulation
Measurement
0
-2
-4
1.7
1.8
1.9
2

(b)

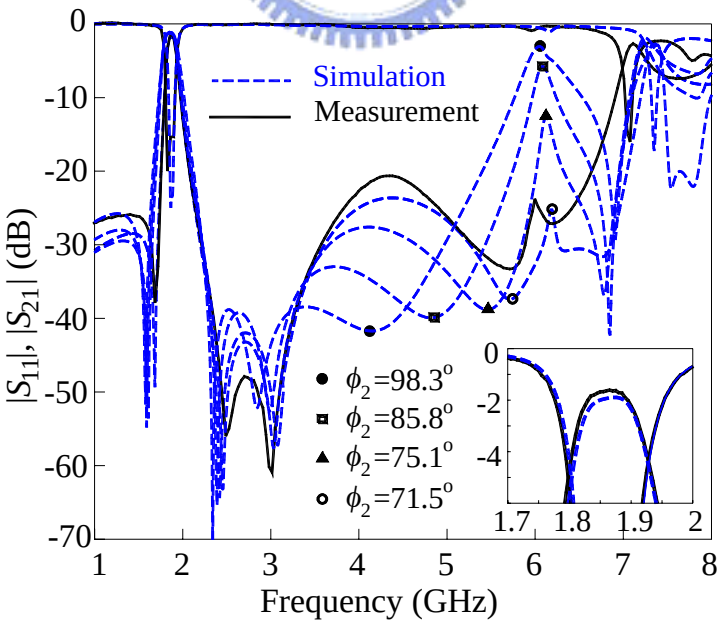
0
-10
-20
-30
-40
-50
-60
-70
1
2
3
4
5
6
7
8
Frequency (GHz)
|S11|, |S21| (dB)
Simulation
Measurement
ϕ2=98.3°
ϕ2=85.8°
ϕ2=75.1°
ϕ2=71.5°
0
-2
-4
1.7
1.8
1.9
2

(c)

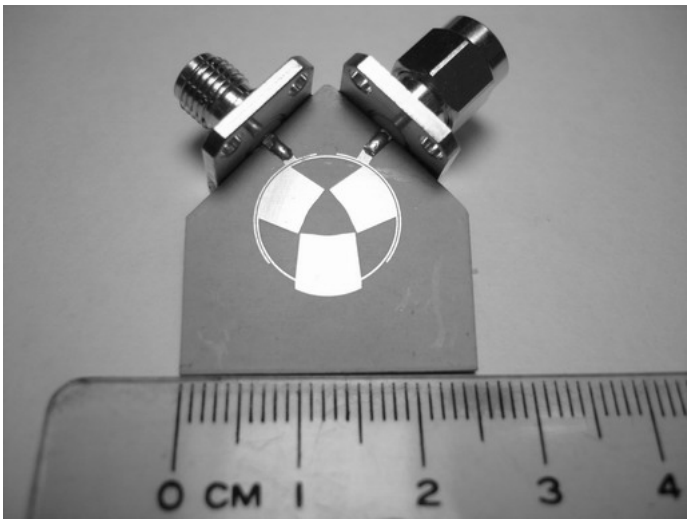

(d)

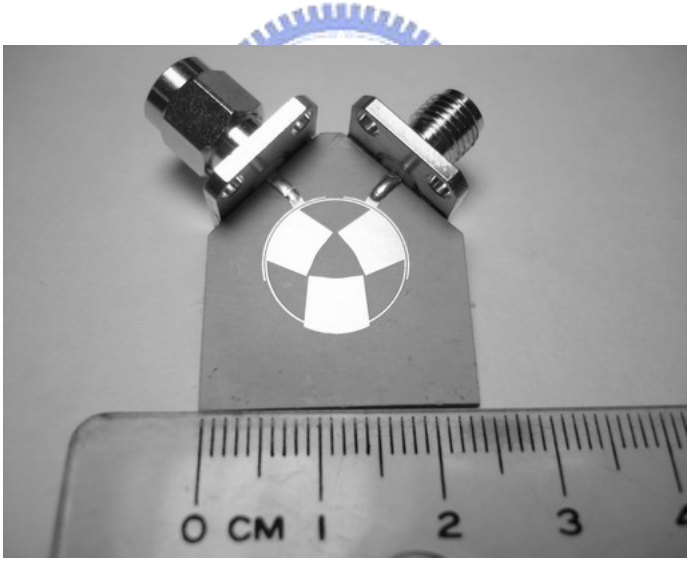

(e)

Figure 3-13 Simulated and measured responses of two PSIRR filter with N = 3. Center frequency f_o = 1.86 GHz. (a) Layout (b) Without spurious suppression. (c) With spurious suppression (d) Photograph of circuit in (b). (e) Photograph of circuit in (c).Substrate: ε_r = 10.2, thickness = 1.27 mm.

Chapter 4

Conclusion

This thesis proposes two miniaturized ring resonators for design of dual-mode bandpass filter. The first is a dual-mode microstrip square loop resonator with the center of each side of the resonator is tapped with an arrow-shap stub. Two dual-mode bandpass filters with bandwidths 3.4% and 3% at center frequency 2.45GHz have been designed and fabricated. The two filters have miniaturized dimensions that use only 46% and 43% of a conventional dual-mode ring bamdpass filter. The measured results have a good agreement with the simulation.

The second miniaturized resonator is periodic stepped-impedance ring resonator (PSIRR). The resonant characteristics of a PSIRR are investigated. As compared with a uniform ring, a PSIRR can not only offer more than 60% in size reduction for dual-mode ring resonator filter design but also the first spurious response at higher than 3.7 times the passband frequency. The amount of size reduction and the distance between passband frequency and first spurious response depend on number of stepped-impedance junctions and impedance ratio of hi-Z to low-Z sections in a ring. The PSIRR with N = 3 has been shown to have the best size reduction for filters with a fractional bandwidth of several percents. Two transmission zeros are generated in the upper stopband and are tunable by adjusting the arm lengths of the line-to-ring coupling structures. For N = 3, one of the zeros can be used to suppress the first spurious response and hence to enhance the bandwidth of and filter performance in the upper stopband. The measured results have a good agreement with the simulation.

Reference

[1] K.Chang, “Microwave Ring Circuits and Antennas.” New York: Wiley, 1996, ch. 3, 7, and 12.

[2] Wolff, “Microstrip bandpass filter using degenerate modes of a microstrip ring resonator,” *Electron Lett.*, vol. 8, no. 12, pp. 302–303, Jun.1972.

[3] L.-H. Hsieh and K. Chang, “Dual-mode quasi-elliptic-function bandpass filters using ring resonators with enhanced-coupling tuning stubs,” *IEEE Trans. Microwave Theory Tech.*, vol. 50, pp. 1340–1345, May 2002.

[4] M. Matsuo, H. Yabuki and M. Makimoto,“Dual-mode stepped-impedance ring resonator for bandpass filter application,” *IEEE Trans. Microwave Theory Tech.*, vol. 49, pp. 1235–1240, July 2001.

[5] A. C. Kundu and I. Awai, “Control of attenuation pole frequency of a dual-mode microstrip ring resonator bandpass filter,” *IEEE Trans. Microwave Theory Tech.*, vol. 49, no. 6, pp. 1113–1117, Jun. 2001.

[6] L. Zhu and K. Wu, “A joint field/circuit model of line-to-ring coupling structures and its application to the design of microstrip dual-mode filter sand ring resonator circuits,” *IEEE Trans. Microwave Theory Tech.*, vol. 47, pp. 1938–1948, Oct. 1999.

[7] C.-Y. Tsai and J.-T. Kuo, "A new miniaturized dual-mode loop filter using coupled compact miniaturized hairpin resonators," in *Asia-Pacific Microwave Conference Proceedings*, Paper 360, New Delhi, India, Dec. 15-18, 2004.

[8] J. S. Hong and M. J. Lancaster,“Microstrip bandpass filter using degenerate modes of a novel meander loop resonator,” *IEEE Microwave Guided Wave Lett.*, vol. 5, pp.371-372, Nov. 1995.

[9] A. Görür, C. Karpuz and M. Akpinar, “A reduced-size dual-mode bandpass filter with capacitively loaded open-loop arms,” *IEEE Microwave Wireless Comp. Lett.*, vol. 13, pp. 385–387, Sep. 2003.

[10] B. T. Tan, J. J. Yu, S. T. Chew, M. S. Leong, and B. L. Ooi, “A miniaturized dual-mode ring bandpass filter with a new perturbation,” *IEEE Trans. Microwave Theory Tech.*, vol. 53, no. 1, pp. 343–348, Jan. 2005.

[11] Ming-Fong Lei, and Huei Wang, “An Analysis of Miniaturized Dual-Mode Bandpass Filter Structure Using Shunt-Capacitance Perturbation,” *IEEE Trans. Microwave Theory Tech.*, vol. 53, no. 3, pp. 861–867, March. 2005.

[12] A. Görür, “A novel dual-mode bandpass filter with wide stopband using the properties of microstrip open-loop resonator,” *IEEE Microwave Wireless Comp. Lett.*, vol. 12, pp. 386–388, Oct. 2002.

[13] U. Karacaoglu, D. Sanchez-Hernandez, I. D. Robertson, and M. Guglielmi, “Harmonic suppression in microstrip dual-mode ring-resonator bandpass filters,” in the *IEEE MTT-S Int. Microwave Symp. Dig.*, pp.1635-1638, 1996.

[14] IE3D simulator (Zeland Software Inc., Jan. 1997).

[15] Jia-Sheng Hong and M. J. Lancaster, “Microstrip Filters for RF / Microwave Application,” Wiley, New York, 2001.